INVESTIGATION OF THE COLLOIDAL BEHAVIOUR OF CARBON BLACK AND PERFLUOROSULFONATED IONOMER IN VARIOUS SOLVENTS

by

Jie Ning

A thesis submitted to the Department of Chemical Engineering

In conformity with the requirements for

The degree of Master of Applied Science

Queen's University

Kingston, Ontario, Canada

(February, 2011)

Abstract

This thesis investigates the interactions between ionomer and carbon black in solution as influenced by different ink parameters. The motivation for this work is to collect necessary data that would lead toward the development of an improved microstructure model of catalyst layer of polymer electrolyte membrane fuel cells. Ionomer aggregation behaviour in solution was investigated at different ionomer concentration, solvent type and solvent composition. Ionomer was found to exist in three forms in solution. Extended molecule chains having a hydrodynamic diameter between 20nm to 30nm. Primary aggregates formed by the hydrophobic interaction of fluorocarbon backbone are around 300nm in diameter. Secondary aggregates formed from electrostatic interaction of side chain ion pairs usually having diameter above 1000nm. Aggregation behaviour of ionomer in different solvents and solvent mixtures at different mixing ratios was also investigated. 1-propanol and 1-propanol/water mixture were found to be the best solvent and solvent mixture among the solvents examined.

Carbon black (CB) particle size distribution in solution was measured under different conditions. A maximum 2hr sonication time is suggested for dispersing CB in solution. Size distribution of CB particles increases with concentration. Water content in the co-solvent mixture influences the particle size distribution of CB. It is suggested that water content should be kept under 50wt% to prevent aggregation of CB particles.

Ionomer is found to adsorb on platinum/carbon (Pt/CB) surface strongly when mixed. The adsorption process comprises a primary adsorption stage and a secondary adsorption stage. At low ionomer concentration, the primary adsorption was found to follow a Langmuir isotherm with maximum surface coverage around 2.66×10^{-3} g ionomer/m^2 Pt/CB. The Pt/CB particle size change due to ionomer adsorption was measured. A maximum size increase around 40nm was found. The size change combined with ionomer molecule geometry estimation implies that only part of the ionomer molecule adsorbed on Pt/CB surface.

Acknowledgements

First of all, I would like to express my deepest sense of gratitude to my supervisor Dr. Aris Docoslis for his patient guide, availability from the initial to final level and his vast knowledge and skill in many areas. I would also like to thank Jeff Wood for his theoretical support, and Matthew Tomkins for his generous help with experiments, as well as other members of Docoslis group for their support and tolerance with the messy lab.

I want to thank my parents for their trust and belief in me. I couldn't have done anything without your support and encouragement.

I would also like to thank Professor: K. Karan, J. Pharoah, B. Peppley as well as Dr. D. Malevich, Ms. Ela Halliop, Mr. Jason Wood and other members of the Fuel Cell Research Centre for their help. Special thanks to Ms. Kathy Fulton at Royal Military College for help with BET measurement and Professor. Hugh Horton from Chemistry Department for XPS data processing

Finally, I would like to acknowledge financial support from Ballard Power Systems Inc.

Table of Contents

List of Figures

List of Tables

List of Symbols

Acronyms

CB: Carbon Black

CED: Cohesive Energy Density

EDL: Electrical Double Layer

DLS: Dynamic Light Scattering

GDL: Gas Diffusion Layer

HSP: Hansen Solubility Parameter

HOR: Hydrogen Oxidation Reaction

LDE: Laser Doppler Electrophoresis

MEA: Membrane Electrode Assembly

MNM: Multi Narrow Mode

ORR: Oxygen Reduction Reaction

PEMFC: Polymer Electrolyte Membrane Fuel Cell

Symbols

A Amplitude

B Baseline

C Ionomer Concentration

C_{eq} Equilibrium Ionomer Concentration

D Diffusion Coefficient (m^2/s)

$D_{\perp}$ Perpendicular Diffusion Coefficient (m^2/s)

$D_{\parallel}$ Parallel Diffusion Coefficient (m^2/s)

E Electric Field (V/m)

E_{thermo} Thermodynamically Predicted Fuel Cell Voltage (V)

E_{vap} Energy of Vaporization (J)

ΔG^M Free Energy of Mixing (J)

ΔH^M Heat of Mixing (J)

ΔH_V Heat of Vaporization (J)

K_{eq} Adsorption Equilibrium Constant

N Total Number of Available Biding Sites

N_A Avogadro Number

R Gas Constant (J/mol·K)

R_H Hydrodynamic Radius (nm)

R_o Interaction Radius

ΔS^M Entropy Change during Mixing (J)

T Temperature (K)

U Electrophoretic Mobility (μmcm/Vs)

V Real Cell Output Voltage (V)

V_M Molar Volume (m^3/mol)

a Particle Radius (nm)

a_n Mie Coefficient

b Adsorption constant

b_n Mie Coefficient

d Adsorption constant

e Elementary Charge (C)

k Boltzmann Constant (m^2kg/s^2K)

k_a	Adsorption Constant
k_d	Desorption Constant
m	Solvent Refractive Index
n	Mode Number
q	Scattering Vector
t	time (s)
v	Velocity (m/s)
γ	Coherence Factor
η_{act}	Activation Overvoltage (V)
η_{ohmic}	Ohmic Overvoltage (V)
η_{conc}	Concentration Overvoltage (V)
τ	Delay Time (s)
λ	Vacuum Wavelength of Laser (nm)
θ	Scattering Angle
η	Viscosity (cP)
Γ_i	Decay Rate
ε_o	Vacuum Permittivity ($C^2/N{\cdot}m$)
ε_r	Relative Permittivity
$1/\kappa$	Debye Length (nm)
ζ	Zeta Potential (mV)
δ	Solubility Parameter ($((cal/cm^3)^{1/2}$)
φ	Volume Fraction
θ_c	Surface Coverage
Γ_{eq}	Equilibrium Surface Coverage
Γ_{max}	Maximum Surface Coverage

Chapter 1

Introduction

1.1 Introduction

Fuel cells are electrochemical devices that convert chemical energy to electrical energy, and are one of the key enabling technologies for the hydrogen economy [Andújar *et al.*, 2009]. Compared to conventional energy sources such as internal combustion engines and batteries, fuel cells combine many of the advantages of both [O'Hayre, 2009]. Fuel cells are more efficient than combustion engines because they convert chemical energy directly into electrical energy; the absence of moving parts also means fuel cells are quiet in operation. There are far fewer undesirable byproducts, such as NOx, COx and particulate emissions, associated with fuel cells; in some cases there are no byproducts at all. Fuel cells have better flexibility than batteries because the system can be scaled independently between power and capacity. They are typically categorized by the electrolyte used [Hoogers, 2003], i.e. Polymer Electrolyte Membrane Fuel Cells (PEMFCs) are thus named because they employ a thin polymer membrane as the electrolyte. PEMFCs are attractive because they operate at low temperatures, have high chemical-to-electrical energy conversion efficiency and high power density, and have easy start-ups [Cleghorn *et al.*, 1998].

The very high power density and other advantages of PEMFCs make them well suited for many applications, including transportation [Prater, 1994], portable power [Chu *et al.,* 2001] and stationary power supply [Millet *et al.,* 2005]. However, cost is the main barrier to the large-scale use of PEMFCs. Studies on the manufacturing cost of fuel cells have identified the catalyst layer as one of the most expensive individual components of a fuel cell system; the noble metal catalyst (platinum) could account for 30%-50% of the cost of a fuel cell system [Wannek *et al.*, 2010]. To attain high efficiency at a low cost, many studies have endeavoured to identify ways to optimize the catalyst layer. These studies have focused on: modeling of the catalyst layer [Baghalha *et al.,* 2010; Marr *et al.,* 1999; Song *et al.,* 2004]; morphology characterization of the catalyst layer by SEM and TEM [Cheng, *et al.,* 1999]; composition optimization of the catalyst layer [Kamarajugadda *et al.,* 2008]. Catalyst layers of PEM fuel cells are produced by applying catalyst ink to both sides of the electrolyte membranes via one of several methods, including spray deposition, painting and screen printing [O'Hayre, 2009].

Since much research has focused on the improvement of the catalyst layer of PEM fuel cells, the catalyst ink that produces the catalyst layers has drawn more and more attention. It has been demonstrated that the solvent composition [Stampino *et al.,* 2009] and ionomer loading [Frey *et al.,* 2004] in the ink dispersion can influence the catalyst layer microstructure, which affects catalyst efficiency and overall fuel cell performance.

An in-depth knowledge of the catalyst ink dispersion could help to improve catalyst layer efficiency and reduce the costs associated with this component.

1.2 Objective and Outline

The properties of the catalyst ink have great influence on the microstructure of the catalyst layer, which will have a significant effect on the fuel cell performance. However, the colloidal interactions between the key ingredients in the catalyst ink formulations are not precisely understood yet. The objective of this thesis project is to investigate the state of dispersion (aggregate size) of ionomer and CB as a function of concentration, solvent type and solvent composition. This thesis will also characterize the adsorption behavior of ionomer and Pt/CB in ink dispersion in terms of the amount of ionomer adsorbed and adsorption configuration. The aggregate size distribution is measured by Dynamic Light Scattering (DLS). The adsorption is measured by Nuclear Magnetic Resonance and other techniques.

Chapter 2 provides background information on fuel cells, namely on the catalyst layer and the Dynamic Light Scattering technique, and presents a literature review on catalyst ink and ionomer aggregation. Chapter 3 lists all the equipment, experimental methods and materials used.

Chapters 4 to 6 present the main results and analysis. Chapter 4 explains the aggregation behaviour of ionomer in a range of ionomer concentrations, solvent types and co-solvent compositions. Chapter 5 explains the aggregation behaviours of CB under different conditions. The aggregation behaviour of Pt/CB is also briefly investigated. Chapter 6 analyses the adsorption of ionomer on the Pt/CB surface when mixed.

Chapter 7 concludes by presenting the results of this project and providing suggestions for future work.

Chapter 2

Background Information

2.1 PEM Fuel Cell

The basic structure of a PEM fuel cell consists of an electrolyte sandwiched between two electrodes, coupled with flow field plates. The two electrodes contain catalyst layers (CL) attached to gas diffusion layers (GDL). The electrolyte-catalyst layer-gas diffusion layer, also referred to as the membrane electrode assembly (MEA), is the heart of a PEM fuel cell [Litster *et al.,* 2004]. The basic fuel cell structure and an enlarged catalyst layer structure view are shown schematically in Figure 2-1. Two electrochemical reactions take place in the catalyst layers. On the anode side, hydrogen gas is passed through to the gas diffusion layer and oxidized into protons and electrons in the catalyst layer. This is known as the *hydrogen oxidization reaction (HOR)*, expressed as:

$$H_2 \rightarrow 2H^+ + 2e^-$$

The protons travel through the hydrated electrolyte to the cathode, and the electrons travel through an external circuit to provide power. On the cathode side, protons and electrons combine with oxygen on the catalyst surface to form water. This reaction is known as the *oxygen reduction reaction (ORR),* expressed as:

$$\frac{1}{2}O_2 + 2H^+ + 2e^- \rightarrow H_2O$$

Therefore, the overall reaction of the fuel cell is:

$$H_2 + \frac{1}{2}O_2 \rightarrow H_2O$$

Under standard conditions[1], the change of the Gibbs free energy of this reaction is -237kJ, which corresponds to a reversible cell voltage of 1.23V (thermodynamically predicted voltage).

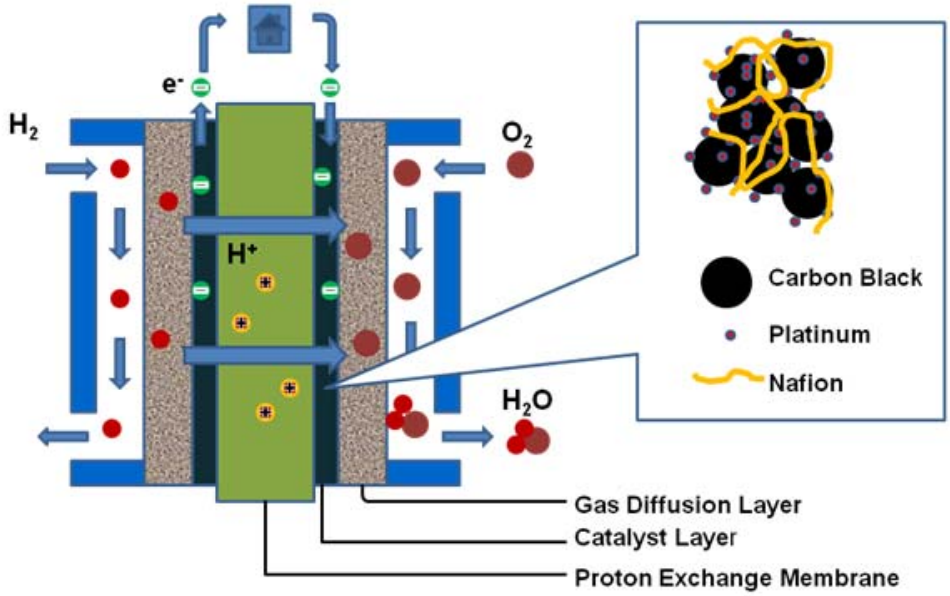

Figure 2-1: Basic fuel cell structure including flow filed plates, gas diffusion layers, catalyst layer.

[1] 1bar and 25°C

In practice, a typical PEM fuel cell's voltage output is less than 1.23V. The real cell voltage output can be written as [O'Hayre *et al.,* 2009]:

$$\boldsymbol{V = E_{thermo} - \eta_{act} - \eta_{ohmic} - \eta_{conc}} \quad (2\text{-}1)$$

where V represents the real fuel cell output voltage; E_{thermo} represents the thermodynamically predicted fuel cell output voltage (1.23V) at standard condition. η_{act}, η_{ohmic}, and η_{conc} represent the three major types of fuel cell losses:

1. Activation losses (η_{act}) are energy required to overcome the activation energy barrier of the reactions in both electrodes. The effects of these losses are mainly in the low current density region. The most effective method to lower the activation barrier is to use a catalyst.
2. Ohmic losses (η_{ohmic}) arise from resistance to ion transfer through the electrolyte, which are the dominant losses at intermediate current density. The ohmic losses can be minimized by making the electrolyte as thin as possible and by using highly conductive materials.
3. Concentration losses (η_{conc}) are due to reactant depletion and product accumulation in the catalyst layer. The effects of these losses are most pronounced in the high current density region. The effect of concentration losses can be minimized by the careful optimization of mass transport inside the fuel cell.

2.1.1 Catalyst Layer

The catalyst layer of a PEM fuel cell is usually a thin (10-30μm) porous layer consisting of a mixture of catalyst and electrolyte material (ionomer) deposited on the surface of the electrolyte. It is made by first formulating a catalyst ink that contains platinum-carbon black mixed with ionomer solution and solvents. The ink is then deposited onto both sides of an electrolyte surface by spray painting, screen printing and/or ink jet printing [Taylor et al., 2007]. Porous carbon paper or carbon cloth is then bonded to the catalyst layer for its protection and to form a conductive current path to the current collector flowfield plate.

Fuel cell reactions can only occur in the catalyst layer where the electrolyte (proton conducting material), catalyst/electrode (electron conducting material) and gas phases are all in contact, known as the "triple-phase zone". The pores in the catalyst layer provide a passway for reactant (H_2, O_2), the electrode materials provide a passway for electron transport, and the electrolyte materials provide a passway for proton transport. Platinum (Pt) is the preferred catalyst [Penner *et al.,* 1995], and carbon black and carbon nanotubes are usually used as catalyst supporting materials. The most commonly used electrolyte material is Nafion^{TM}, made by DuPont, generated by the copolymerization of a perfluorinated vinyl ether comonomer with tetrafluoroethylene [Mauritz *et al.,* 2004].

A significant amount of research has been conducted on the optimization of catalyst layers of PEM fuel cells. It has been found that the substitution of expensive platinum catalysts with other materials can reduce the cost of the catalyst [Grigoriev *et al.,* 2007; Karyakin *et al.,* 2002; Wang, 2005]. Additionally, microstructure studies have helped to improve mass transport and catalyst utilization [Farhat, 2004; Khajeh-Hosseini-Dalasm *et al.,* 2010; Wang *et al.,* 2004].

2.1.2 Catalyst Ink

Significant efforts have been undertaken to investigate the effects of catalyst ink properties on the performance of PEM fuel cells. Research on catalyst ink composition [Fernández *et al.,* 2005; Kim *et al.,* 2004, Wang *et al.,* 2007], ink preparation methods [Shin *et al.,* 2002] and ionomer loading [Uchida *et al.,* 1995, 1998] have shown that interactions between catalyst ink materials, and the aggregation behaviour of carbon-supported platinum (Pt/CB) and ionomer in the ink solution, can affect the area of the active reaction site (triple phase zone), mass transport and ion transport in a PEM fuel cell. Catalyst ink typically consists of carbon-supported platinum and ionomer in a co-solvent mixture of water and propanol. When dispersed in a solution, the Pt/CB and ionomer tend to aggregate and interact with each other.

2.1.3 Ionomer

The most commonly used ionomer in PEM fuel cells is Nafion^{TM} from DuPont, which are the first commercially-available Perfluorosulfonated ionomer (PFSI). The distinct properties of Nafion^{TM}, with respect to stability, solubility and ionic conductivity, make it an excellent material for PEM fuel cells [Wilson *et al.*, 1992]. The structure of Nafion^{TM} consists of a hydrophobic tetrafluoroethylene (Teflon) backbone and a perfluorovinyl ether group terminated with sulfuric acid groups, as shown in figure 2 [Deluca *et al.*, 2006].

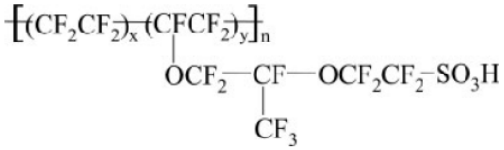

Figure 2-2 chemical structure of Nafion

When exposed in water, the sulphonic group in its hydrated form ($SO_3^-H_3O^+$) allows effective proton transport across the membrane. The molecular shape and aggregation state of ionomer were characterized by many measurement techniques. A cylindrical (rod-shaped) molecule for ionomer in a solution, with varied lengths and in different solvents, was proposed by Aldebert *et al.,* [1986] by using small angle neutron scanning technique. The radius of the cylindrical shaped molecule was then resolved to be around 20Å by small angle scattering studies [Loppinet *et al.,* 1997]. The aggregation state of

ionomer in a solution is determined by the polarity of the solvent and its ability to dissolve the polymer backbone [Dubin *et al.,* 1994]. This can be distinguished into three types of solutions [Jiang *et al.,* 2001]:

1. Ionomer solutions in non-polar solvents are characterized by a concentration-dependent equilibrium between intra- and interchain aggregation due to electrostatic attraction between nonionized ion-pairs on the solvated backbone.
2. Ionomer solutions in polar solvents that are able to dissolve the polymer backbone are characterized by rather extended polymer chains similar to weakly charged polyelectrolytes.
3. Ionomer solutions in polar solvents in which the analogous neutral polymer is not soluble are characterized by polymer-solvent separation, resulting in colloidal dispersion.

The aggregate size distribution of ionomer in various solvents and solvent mixtures has been primarily investigated using the Dynamic Light Scattering (DLS) technique [Chen *et al.,* 2008; Cirkel *et al.,* 1999; Jiang *et al.,* 2001; Lee *et al.,* 2004; Lin *et al.,* 2005]. The hydrodynamic radius of a single ionomer molecule is found to be less than 100nm [Chen *et al.,* 2008]. Different ionomer aggregate sizes were found owing to two kinds of aggregation processes: a smaller aggregate due to hydrophobic interactions of the fluorocarbon backbone, and a larger secondary aggregate arising from electrostatic

attraction between ion-pairs [Jiang *et al.,* 2001; Lee *et al.,* 2004;]. The existence of the two aggregate types was also confirmed by viscoelasticity analysis and zeta potential measurement of the ionomer solution [Lee *et al.,* 2004, Zhang *et al.,* 2008]. Schematic view of the ionomer molecules and different forms of aggregates are shown in Figure 2-3 below [Szajdzinska-Pietek *et al.,* 1994]:

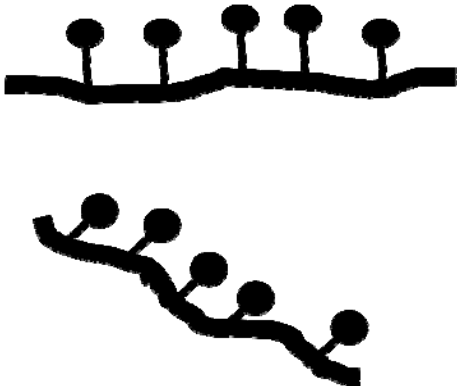

(a)

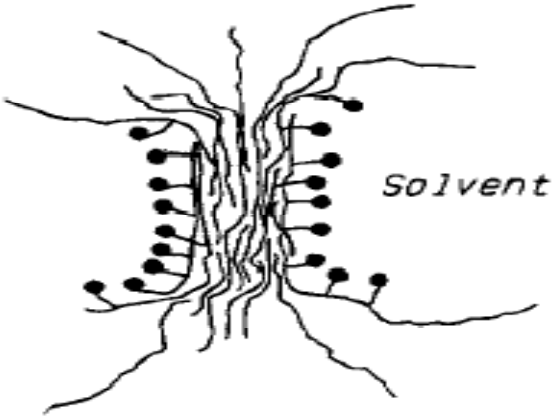

(b)

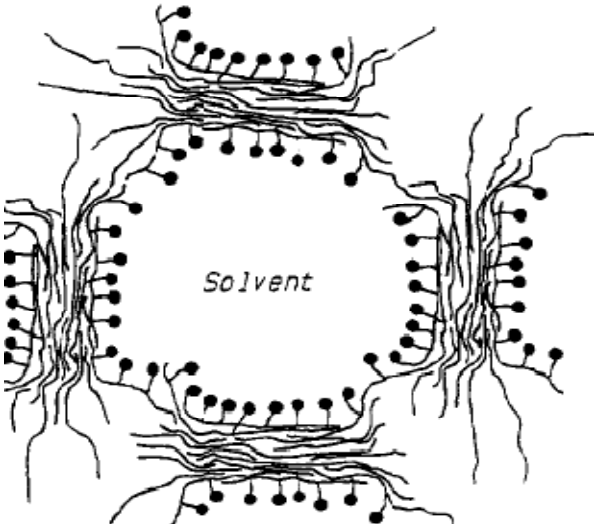

(c)

Figure 2-3 Aggregation forms of ionomer: (a) ionomer molecules in solvent, long bold line represents ionomer backbone, spheres with short tail represent ionomer side chain; (b) ionomer primary aggregate, formed through interactions of ionomer molecule backbones; (c) ionomer secondary aggregate, formed through interactions of ionomer size chains. [taken from Szajdzinska-Pietek *et al.,* 1994]

2.2 Dynamic Light Scattering

Dynamic Light Scattering (DLS), also known as Photon Correlation Spectroscopy (PCS), is a technique used to determine particle size by examining the diffusion rates (i.e. Brownian motion) of suspended particles [Chu, 2008]. For sample particles dispersed in a solution, a monochromatic light, such as a laser, is shot at the sample solution, and a detector typically positioned at a fixed angle measures the scattered light intensity. The measured intensity of the scattering light will fluctuate since the particles are undergoing

Brownian motion [Maurer-Spurej *et al.,* 2006]. Across a long time interval, the intensity of the scattering light will appear to randomly fluctuate around a certain mean value. When intensity of scattering light is viewed at a small time scale, it appears that the intensity signals are strongly correlated. This correlation is a consequence of the fact that particles are at a position very near to the position occupied a very short time ago. The rate of change of the signal depends on the rate of change of the position of the particles. Large particles moving more slowly will result in a slow decay of correlation, and small particles moving faster will result in a fast decay of correlation.

In Dynamic Light Scattering, all information regarding the motion of the particle in the solution is contained in the correlation curve. For a sample consisting of mono-dispersed particles, the correlation curve can be fit to a single exponential form, where I is the intensity, t is the time, τ is the delay time, B is the baseline, A is the amplitude, and D is the diffusion coefficient [Kaszuba *et al.,* 2007]:

$$\boldsymbol{G(\tau) = \int I(t)I(t+\tau)dt = B + Ae^{-2q^2D\tau}} \quad (2\text{-}2)$$

The scattering vector (q) is defined in Goldburg [1999], where *n* is the solvent refractive index, λ is the vacuum wavelength of the laser, and θ is the scattering angle:

$$\boldsymbol{q = \frac{4\pi n}{\lambda} sin\left(\frac{\theta}{2}\right)} \quad (2\text{-}3)$$

The above two equations allow the particle diffusion coefficient to be calculated. The hydrodynamic radius, which is defined as the radius of a hard sphere that diffuses at the same rate as the particle under examination, is calculated using the Stokes-Einstein equation:

$$\boldsymbol{R_H = \frac{k_B T}{6\pi\eta D}} \tag{2-4}$$

The distribution of particle size is calculated by an approximation of the continuous autocorrelation function (equation 2-2). The new equation [Malvern Technical Support Library] is expressed as:

$$\boldsymbol{G_k(\tau_k) = \sum_{i=0} I(t_i) I(t_i + \tau_k)} \tag{2-5}$$

The Siegert relation holds true when the intensity statistics of measured signals are Gaussian; the normalized intensity autocorrelation function can be expressed as:

$$\boldsymbol{G(\tau) = 1 + \gamma g(\tau)^2} \tag{2-6}$$

where $g(\tau)^2$ is the field autocorrelation function and γ is the coherence factor. Data inversion consists of finding the appropriate distribution of exponential decay functions that best describe the measured field correlation function. The fitting function for $g(\tau)_k$ consists of a summation of single exponential functions, constructed as a grid of exponential with decay rate Γi, where $\Gamma = Dq^2$, A_i is the area under the curve for each exponential contribution:

$$g_k^{fit} = \sum_i A_i e^{\Gamma_i \tau_i} \tag{2-7}$$

The best fit is found by minimizing the deviation of the fitting function from the measured data points. This is expressed as:

$$\xi^2 = \sum_k \left(g_k - g_k^{fit}\right)^2 \sigma_k = \sum_k (g_k - \sum_i A_i e^{\Gamma_i \tau_i})^2 \, \sigma_k \tag{2-8}$$

where σ_k is a factor to emphasis on strong correlations. The solution is achieved first by minimizing ξ^2 with respect to each A_i, and then solving the equations. The correlation function of a spherical particle with radius R_i and decay rate Γ_i is:

$$\Gamma_i = (D_i q^2) = \left(\frac{k_B T}{6\pi\eta R_i}\right)\left(\frac{2\pi n}{\lambda} sin\left(\frac{\theta}{2}\right)\right)^2 \tag{2-9}$$

And the intensity particle size distribution is calculated by:

$$R = \frac{\sum A_i R_i}{\sum A_i} \tag{2-10}$$

The calculated intensity distribution can be converted to volume distribution by employing Mie theory [Mie, 1908]. The scattering intensity according to Mie theory, where $|S_1|^2$ and $|S_2|^2$ are scattered intensities, is [Van de Hulst, 1957;]

$$F(\theta, \varphi) = |S_1(\theta)|^2 sin^2\varphi + |S_2(\theta)|^2 cos^2\varphi \tag{2-11}$$

The complex scattering amplitudes for two orthogonal directions of incident polarization can be written as [Wiscombe, 1980]:

$$S_1(\theta) = \sum_{n=1}^{\infty} \frac{2n+1}{n(n+1)} [a_n \pi_n \cos\theta + b_n \tau_n \cos\theta] \tag{2-12}$$

$$\boldsymbol{S_2(\theta) = \sum_{n=1}^{\infty} \frac{2n+1}{n(n+1)} [b_n \pi_n \cos\theta + a_n \tau_n \cos\theta]} \quad (2\text{-}13)$$

In the above equations, n is the mode number, a_n and b_n are the Mie coefficients. π_n and τ_n are defined using nth order Legendre polynomials (Pn) as defined below:

$$\boldsymbol{\pi_n \cos\theta = \frac{1}{\sin\theta} P_n^1 \cos\theta} \quad (2\text{-}14)$$

$$\boldsymbol{\tau_n \cos\theta = \frac{d}{d\theta} P_n^1 \cos\theta} \quad (2\text{-}15)$$

The Mie coefficients can be expressed as [Du, 2004; Shen, et al., 2005;]:

$$\boldsymbol{a_n = \frac{\psi_n(\alpha)\psi_n'(m\alpha) - m\psi_n'(\alpha)\psi_n(m\alpha)}{\zeta_n(\alpha)\psi_n'(m\alpha) - m\zeta_n'(\alpha)\psi_n(m\alpha)}} \quad (2\text{-}16)$$

$$\boldsymbol{b_n = \frac{m\psi_n(\alpha)\psi_n'(m\alpha) - \psi_n'(\alpha)\psi_n(m\alpha)}{m\zeta_n(\alpha)\psi_n'(m\alpha) - \zeta_n'(\alpha)\psi_n(m\alpha)}} \quad (2\text{-}17)$$

where m is the refractive index of the particle to the medium, α is the particle size parameter (defined as $\alpha = \frac{\pi x}{\lambda}$, where x is the particle diameter), and λ is the vacuum wavelength of the incident light. The data measured from DLS provides the amount of light scattered by the particle of a certain diameter, and Mie scattering formulas provide information on how much intensity is scattered by a particle of a certain diameter. The number distribution can be calculated as:

$$\boldsymbol{I(x) = N(x)M(x)} \quad (2\text{-}18)$$

where I(x) is the intensity distribution, M(x) is the Mie scattering and N(x) is the number distribution. The volume distribution V(x), can be then calculated by assuming a spherical particle:

$$\boldsymbol{V(x) = \frac{4}{3}\pi\left(\frac{x}{2}\right)^3} \tag{2-19}$$

2.3 Electrophoretic Light Scattering

When a particle is immersed in solution, the presence of the charges on the particle surface generate an electric field, which attracts the oppositely charged ions and repels like charges, results in an increased concentration of opposite charges near the particle surface. As one moves away from the particle surface, the heterogeneous ions distribution will become homogeneous. The layer of heterogeneous distributed ions is known as Electrical Double Layer (EDL) and the distance that a homogeneous distribution is obtained is called the Debye length (1/κ), defined as [Russel *et al.,* 1989]

$$\boldsymbol{Debye\ Length = \frac{1}{\kappa} = \sqrt{\frac{\varepsilon_o \varepsilon_r k_B T}{2000 N_A e^2 I}}} \tag{2-20}$$

where ε_o is the permittivity of vacuum, ε_r is the relative permittivity, k_B is the Boltzmann constant, T is the temperature in kelvins, N_A is the Avogadro number and e is the elementary charge. The EDL comprised of a Stern layer and a diffuse layer [Tandon et al., 2008]. The Stern layer consists of strongly bounded ions and diffuse layer consists of

ions less firmly associated. Within the double layer exists a boundary which ions inside the boundary will move with particles when particles moving. The electric potential at this boundary is defined as zeta potential. An illustration of the double layer and zeta potential is shown in figure 2-4 below

[Malvern http://www.malvern.com/LabEng/technology/zeta_potential/zeta_potential_LDE.htm]

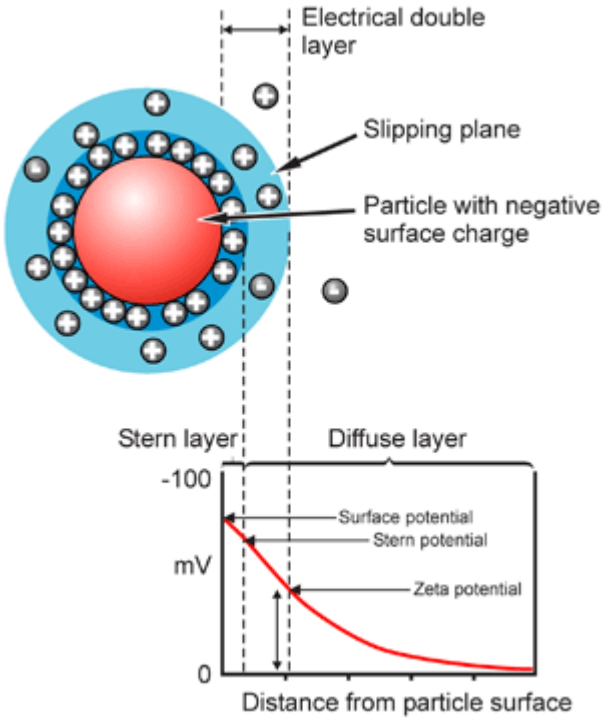

Figure 2-4 Schematic representation of Electrical Double Layer and zeta potential.

Zeta potential values provide valuable information on the electrostatic stability of colloidal system. If the particles in the colloidal system have large absolute zeta potential

values, they tend to repel each other and the system is stable. If the absolute zeta potential values of the particles are low, it is possible for the particles to aggregate in the solution

Charged particles in solution subject to an applied electric field will migrate to the electrode of opposite charge, experiencing a viscous force that opposes their movement. The particles will move at constant velocity *v* when the two forces reached equilibrium. The speed is directly proportional to the magnitude of the field, *E*. The constant of proportionality is called the electrophoretic mobility, *U* [Ware, 1974]

$$\boldsymbol{v = UE} \tag{2-21}$$

The electrophoretic mobility can be expressed as [Arrio *et al.,* 1984]:

$$\boldsymbol{U = \frac{2\varepsilon_o \varepsilon_r \zeta f(\kappa a)}{3\eta}} \tag{2-22}$$

where ε_o is the permittivity of vacuum, ε_r is the relative permittivity of the medium, η is the viscosity of the solution, ζ is the zeta potential, κ is the inverse Debye length and a is the particle radius. f(κa) is the Henry function [Henry, 1931], where

$$\boldsymbol{f(\kappa a) = \frac{3}{2} - \frac{9}{2\kappa a} + \frac{75}{2\kappa^2 a^2} - \frac{330}{\kappa^3 a^3},\ \kappa a > 1} \tag{2-23}$$

$$\boldsymbol{f(\kappa a) = 1 + \frac{(\kappa a)^2}{16} - \frac{5(\kappa a)^3}{48} - \frac{(\kappa a)^4}{96} + \frac{(\kappa a)^5}{96} - \left[\frac{(\kappa a)^4}{8} - \frac{(\kappa a)^6}{96}\right] e^{\kappa a} \int_{\infty}^{\kappa a} \frac{e^{-1}}{t} dt, \kappa a < 1} \tag{2-24}$$

2.4 Solubility Parameter

Hildebrand and Scott [Hansen, 2000] first used the term 'solubility parameter' to predict the degree of interaction between materials. The Hildebrand solubility parameter is defined as:

$$\boldsymbol{\delta} = \left(\frac{\boldsymbol{E_{vap}}}{\boldsymbol{V_M}}\right)^{\mathbf{1/2}} = \left(\frac{\boldsymbol{\Delta H_v - RT}}{\boldsymbol{V_M}}\right)^{\mathbf{1/2}} \tag{2-25}$$

where V_M is the molar volume of the pure solvent, and E_{vap} is the energy of vaporization. The term E_{vap} / V_M is defined as the cohesive energy density (CED), which is the amount of energy needed to completely remove unit volume of molecules from contact to infinite separation, and is also equal to the heat of vaporization divided by molar volume. The Hildebrand solubility parameter is useful in predicting non-polar and slightly polar (dipole moment<2 debye) systems without hydrogen bonding.

For solution processes to occur spontaneously, thermodynamics require that the free energy of mixing be zero or negative. The free energy change of mixing for a solution is expressed by the equation:

$$\boldsymbol{\Delta G^M = \Delta H^M - T\Delta S^M} \tag{2-26}$$

where ΔH^M is the heat of mixing, T is the absolute temperature, and ΔS^M is the entropy change during the mixing process. Hildebrand and Scott propose the heat of mixing as:

$$\boldsymbol{\Delta H^M = \varphi_1 \varphi_2 V_M (\delta_1 - \delta_2)^2} \tag{2-27}$$

where subscript 1 and 2 refer to solute and solvent. φ is the volume fraction and V_M is molar volume of the mixture [Gharagheizi, 2007; Hansen, 2000]. The above equation was found to be incorrect because it allows the heat of mixing to be positive only. Patterson and his colleagues have corrected the equation so that its right hand side is correct for the expression of the noncombinatorial free energy of a solution:

$$\boldsymbol{\Delta G^{M}_{noncomb} = \varphi_1 \varphi_2 V_M (\delta_1 - \delta_2)^2} \quad (2\text{-}28)$$

where $\Delta G^{M}_{noncomb}$ includes all free energy effects other than the combinatorial entropy of the solution occurring due to the simple mixing of components. This equation can be differentiated to express both positive and negative heat of mixing [Hildebrand et al., 1962; Patterson et al., 1962].

However, when a polar solvent is involved, predictions of the Hildebrand solubility parameter are less accurate, since the total energy of vaporization of a liquid consists of several individual parts [Hansen, 1967; Hansen *et al.,* 1967]. These arise from the dispersion force, permanent dipole force and hydrogen bonding force, which are the three major types of interaction in common organic materials [Hansen, 2000]. Ethanol and nitromethane, for example, have similar Hildebrand solubility parameters (26.1 and 25.1 $MPa^{1/2}$), but their solubility is quite different. Ethanol is water soluble while nitromethane is not. As such, a more widely used solubility parameter to predict the solubility of a polymer is proposed by Hansen. The basic equation governing the Hansen Solubility

Parameter (HSP) is that the total cohesive energy E_{vap} is the sum of all individual energies of which it is composed,

$$\boldsymbol{E_{vap} = E_D + E_P + E_H} \tag{2-29}$$

divided by the molar volume,

$$\boldsymbol{E_{vap}/V_M = E_D/V_M + E_P/V_M + E_H/V_M} \tag{2-30}$$

and with the square of the total solubility parameter as a sum of each component:

$$\boldsymbol{\delta_{Total}^2 = \delta_D^2 + \delta_P^2 + \delta_H^2} \tag{2-31}$$

Chapter 3

Materials and Methods

3.1 Ionomer Solution Preparation

5wt%, Perfluorosulfonic acid-PTFE copolymer (Nafion^{TM}) solution was purchased from Alfa-Aesar, containing a mixture of water, 1-propanol and ethanol. 3-methyl-1-butanol (iso-amyl alcohol), 1-propanol, isopropanol, ethylene glycol, n-butyl acetate, dimethyl sulfoxide (DMSO) were purchased from Sigma Aldrich. All the solvents were filtered through 0.2μm nylon filters before use.

Ionomer dry films were prepared by vacuum drying the as-received Nafion^{TM} stock solution at 25^{o}C for 12 hr. The obtained ionomer films were then dissolved in:

1. 1-propanol and water mixture at 1:1 weight ratio to form ionomer solutions with ionomer concentrations ranging from 0.1wt% to 10wt%.
2. 3-methyl-1-butanol (iso-amyl alcohol), 1-propanol, isopropanol, ethylene glycol, n-butyl acetate, Dimethyl sulfoxide (DMSO) and water to form 0.1wt% ionomer solutions in different pure solvents.
3. 3-methyl-1-butanol/water, 1-propanol/water, isopropanol/water, n-butyl acetate/water, DMSO/water at 4:1, 2:1, 1:1 and 1:2 weight ratio to form 0.1wt% ionomer solutions in different co-solvent mixtures.

The dissolved ionomer solutions were sonicated for 0.5hr and then left to equilibrium for 12 hrs.

3.2 Carbon Black Dispersion Preparation

Carbon black powder, Vulcan XC-72, was obtained from Cabot Corporation. Carbon black dispersions were prepared by mixing CB powder with the following solvents:

1. 1-propanol, isopropanol and DMSO at 0.01wt% CB concentration. The mixed solutions were sonicated for 12hrs.
2. 1-propanol, isopropanol and DMSO with CB concentration ranging from 0.0001wt% to 1wt%. The mixed solutions were sonicated for 4hrs.
3. 1-propanol and water mixture at 4:1, 2:1, 1:1 and 1:2 1-propanol to water weight ratio. The mixed solutions were sonicated for 4hrs.

A VWR sonication bath (Model 50D, VWR International) was used for the sonication of samples.

3.3 Pt/CB and Ionomer Mixed Solution Preparation

10wt% Pt on Vulcan XC-72 was received from E-TEK Inc., MA, USA. The Pt/CB powder was mixed with 1-propanol/water at 1:1 weight ratio at 0.001wt% and 0.1wt% Pt/CB concentration. The mixtures were sonicated for 0.5hr.

Ionomer dry films were prepared by vacuum drying the as-received Nafion^{TM} stock solution at 25^{o}C for 12 hrs. The obtained dry films were dissolved in 1-propanol/water at 1:1 weight ratio to form ionomer solutions with ionomer concentration ranging from 0.01wt% to 2wt%. The dissolved ionomer solutions were sonicated for 0.5hr and left to equilibrate for 12hrs.

The prepared ionomer solutions were mixed with 0.001wt% and 0.1wt% Pt/CB dispersions. The mixtures were sonicated for 0.5hr.

3.4 Dynamic Light Scattering Measurements

The aggregate/particle size distributions of prepared samples and sample mixtures were measured by the Zetasizer Nano ZS system (Malvern Instrument Ltd), equipped with a 633nm He-Ne laser. A glass cuvette with a square aperture was used as sample holder. Sample heights in the cuvette were kept between 10mm and 15 mm to obtain best optical measurement. All samples were measured at 20^{o}C and a 5min equilibrium time was applied to ensure samples reached such temperature.

In the experiments, all measurement results were analyzed by Dispersion Technology Software 5.03 (Malvern Instrument Ltd). A Multi Narrow Mode (MNM) was applied to calculate the size distribution data.

3.5 Laser Doppler Velocimetry Measurement

Zeta potential values of the ionomer solution were measured by the Zetasizer Nano ZS system (Malvern Instrument Ltd). A Universal Dip Cell was used for the measurement.

3.6 Viscosity Measurement

The viscosities of the ionomer solutions and Pt/CB and ionomer mixtures were measured by an AR 2000 viscometer (TA Instruments) with the application of a 40mm stainless steel parallel plate geometry. The measured viscosity data was fitted linearly and the viscosity value of the mixture was obtained at zero shear rate by extrapolated the fitted line.

3.7 Nuclear Magnetic Resonance Measurement

19F-NMR measurements were performed on a Bruker Avance-400 400MHz spectrometer located in the Chemistry Department at Queen's University. The prepared 1mL Pt/CB and ionomer mixtures were centrifuged. A VWR galaxy 7D centrifuge

(VWR International) was used for the centrifugation of samples. Samples were centrifuged at 10000rpm (7.2g) for 90min. 500µL of the supernatant were transferred to 5mm standard NMR tubes. 50µL of Deuterium-oxide was then added to the tube to provide a lock. A Stem Coaxial Insert loaded with trichlorofluoromethane ($CFCl_3$) was inserted into the NMR sample tubes to provide an internal reference. The same coaxial insert was used for all measurements.

ACD 1D NMR software (Advanced Chemistry Development Inc.) was used for data analysis.

Chapter 4

Aggregation Behaviour of Ionomer in Solution

In this chapter the aggregation behaviours of ionomer in solution is examined. The influences of ionomer concentration, solvent type and co-solvent composition on the aggregate size of ionomer is investigated using the Dynamic Light Scattering (particle size) and Laser Doppler electrophoresis (zeta potential) techniques.

4.1 Aggregation Behaviour of Ionomer in Solution as a Function of Ionomer Concentration

The aggregate size distribution of ionomer in solution at different ionomer concentrations was examined. Solvent composition for ionomer solutions is chosen as 1-propanol to water at 1:1 weight ratio. The solvent composition was chosen to be similar to the ionomer stock solvent composition. Viscosities of ionomer samples were measured and used to calculate the aggregate size with the Stokes-Einstein equation. The measured viscosities of solutions at different concentrations are shown in Figure 4-1 below:

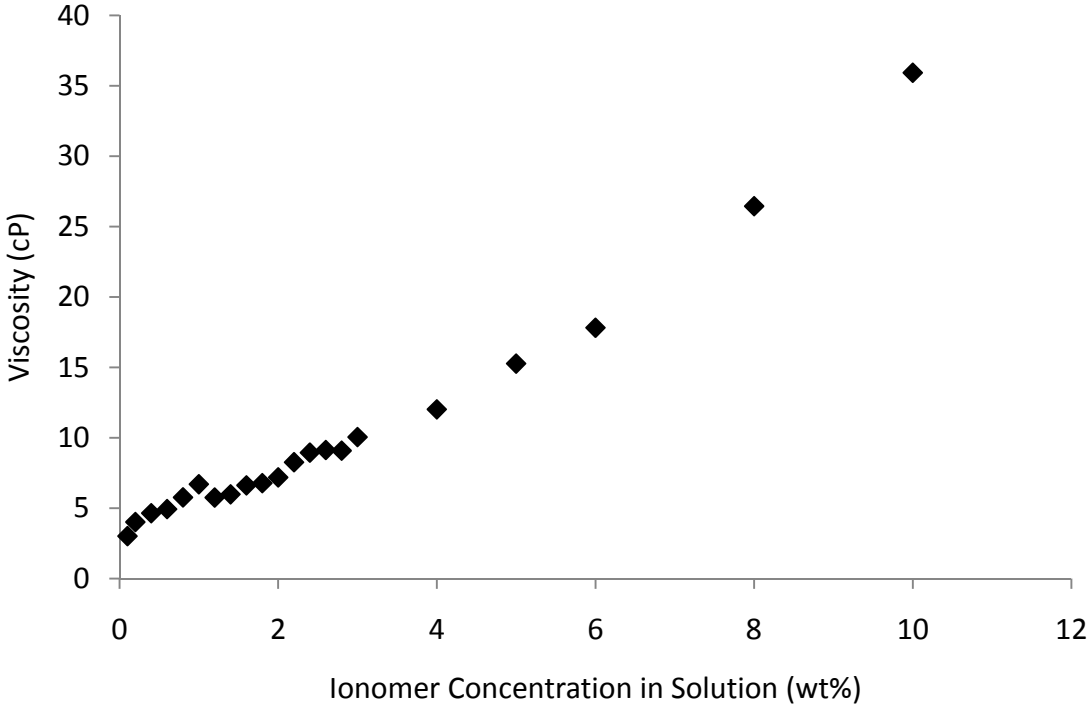

Figure 4-1 Ionomer solution viscosities in 1-propanol/water mixture at 1:1 weight ratio at different concentrations.

Ionomer aggregate size distributions were measured by DLS, and the results size distributions as a function of scattered intensity were converted into volume percent distribution by Mie theory. An example of measured intensity aggregate size distributions and converted volume distributions of 0.1wt% and 8wt% ionomer solutions is shown in Figure 4-2 below:

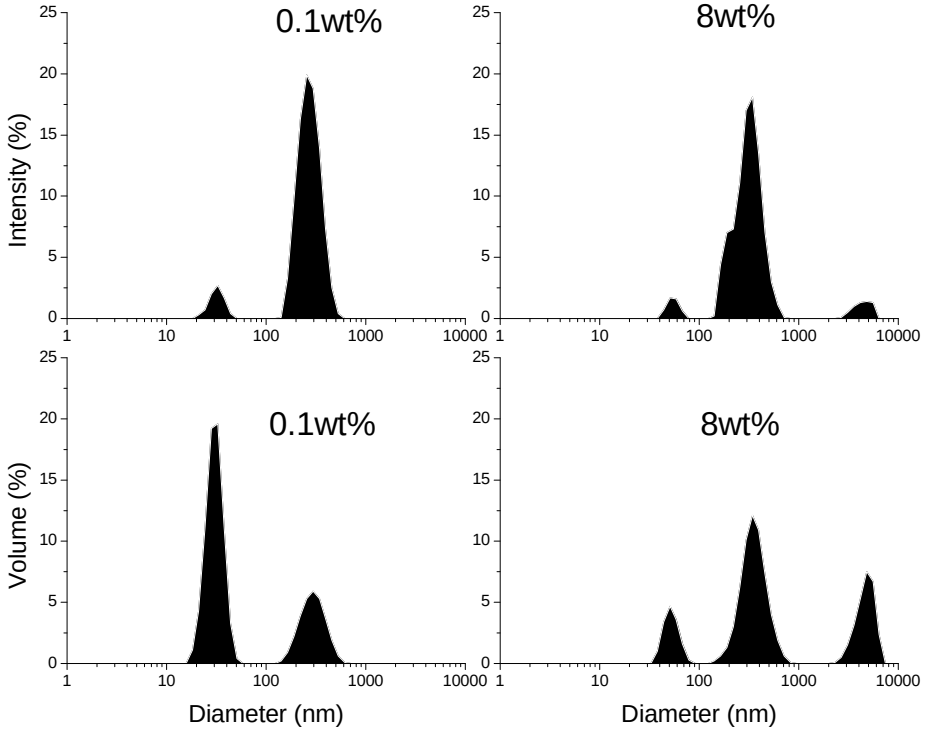

Figure 4-2 Intensity and volume aggregate size distributions of 0.1wt% and 8wt% ionomer solutions.

Different groups of aggregates were found in ionomer solutions in the concentration range examined. Previous dynamic light scattering studies of ionomer in various solvents, including water, methanol/water, ethanol/water, isopropanol/water and DMF have shown multimodal and bimodal particle size distributions. Typically, the small particle size (<100nm) group corresponded to the single molecular chain, as shown in Figure 2-3 (a).

Medium size particles (~500nm) and large size particles (>1000nm) were also observed and related to ionomer aggregate. The medium size particles were assigned to primary rodlike aggregates, which are formed through hydrophobic interaction of fluorocarbon backbone. Large size particles were assigned to secondary aggregates which formed by ionic interactions of primary aggregates [Crikel *et al.,* 1999; Jiang *et al.,* 2001; Kang *et al.,* 2010; Lee *et al.,* 2004; Lin *et al.,* 2005; Wang *et al.,* 2007]. A group of ionomer with hydrodynamic diameter between 20nm to 30nm was found in solution at most concentrations. The size distribution and volume distribution of this ionomer group are shown in Figure 4-2. This group of ionomer is the dominant ionomer group (approximately 70 to 90 volume percent) in solution, between 0.1wt% to 3wt% ionomer concentration. At between 3wt% and 5wt%, the volume percentage of the ionomer in molecular chain form dropped rapidly, from 70% to 20%. At concentrations above 5wt%, only a fraction of ionomer remained as molecular chains.

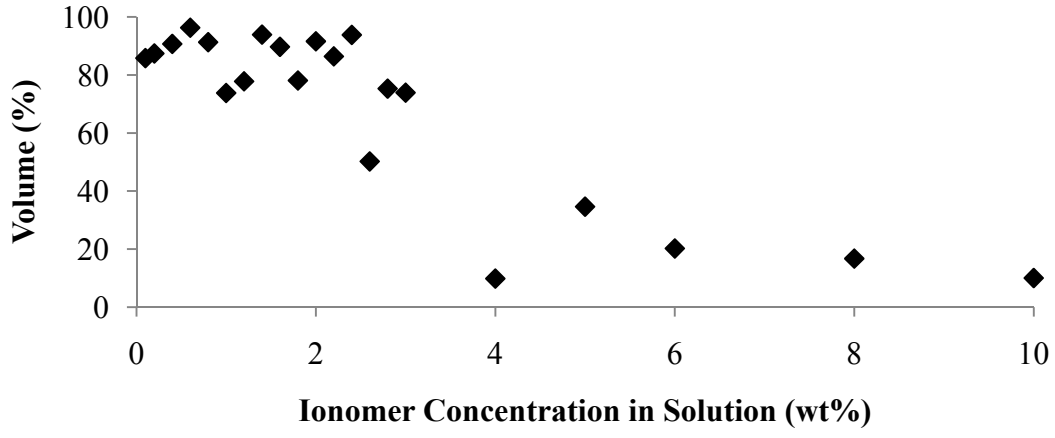

(a)

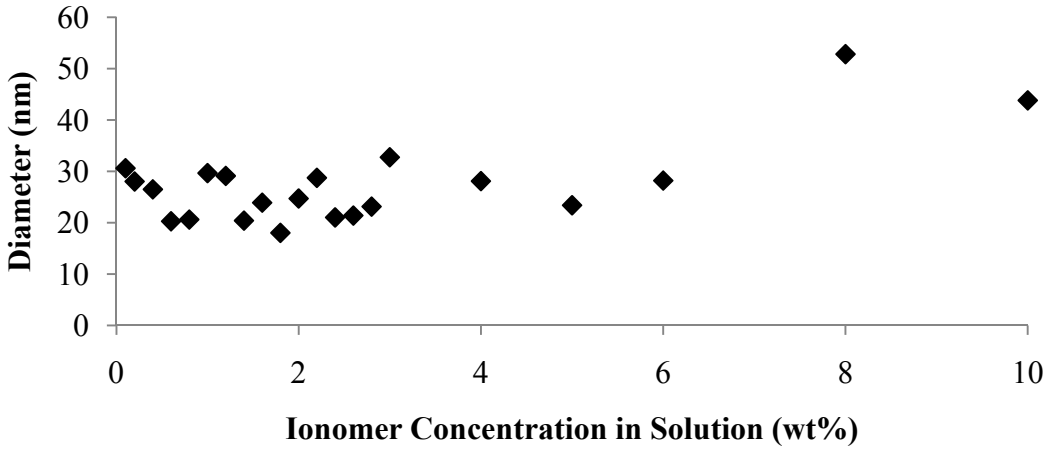

(b)

Figure 4-3 Ionomer molecular chain size and volume distributions: (a) ionomer molecular chain size distribution – Most ionomer have hydrodynamic diameters between 20nm to 30nm, with some exceptions at higher ionomer concentrations (8wt% and 10wt%); (b) ionomer molecular chain volume distribution – Most ionomer exist in molecular form at concentrations below 3wt%, but above that, the fraction of ionomer in molecular form decreases as ionomer concentrations increase.

A group of ionomer with hydrodynamic diameter around 300nm was also found in the solution. Since the hydrodynamic diameter of this group is much greater than the molecular form ionomer, it is believed that these are ionomer primary aggregates, formed from ionomer molecules through the hydrophobic interaction of the ionomer backbone [Szajdzinska-Pietek et al., 1994]. The volume fraction of these primary aggregates is small, between 0.1wt% and 3wt% ionomer concentrations. Above 3wt%, more than 50 percent of ionomer in the solution were in primary aggregate form. The size and volume distributions of these aggregates are shown in Figure 4-4 below:

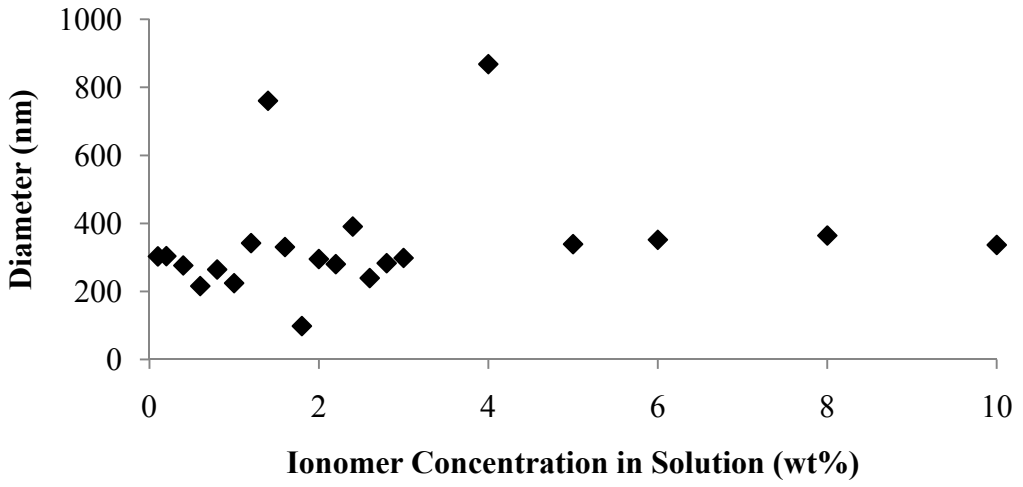

(a)

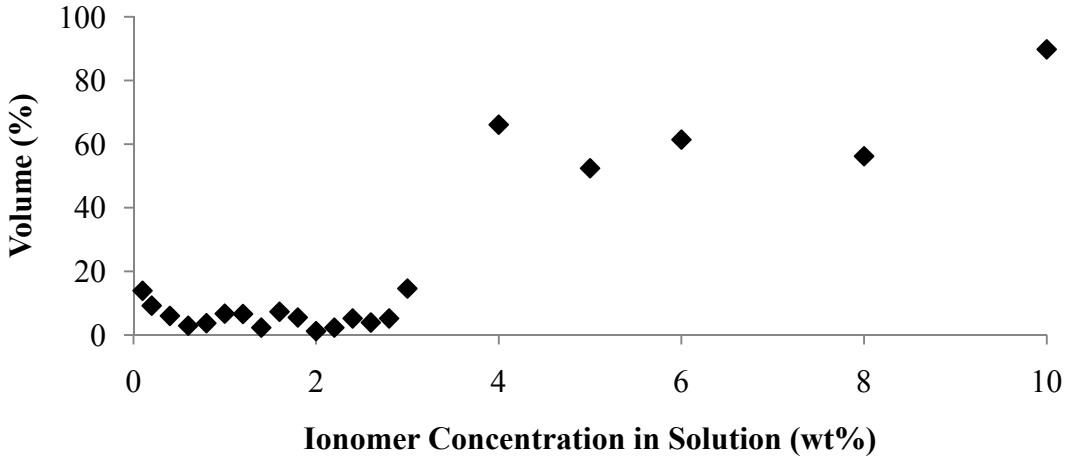

(b)

Figure 4-4 Ionomer primary aggregates, size and volume distributions. (a) hydrodynamic diameter of primary aggregates – Most primary aggregates, with few exceptions, have

diameters around 300nm, which is distinct from the size of ionomer molecules; (b) volume distribution of primary aggregates – At ionomer concentrations below 3wt%, the volume percentage of primary aggregates ranges from 0 to 10 of the total ionomer in solution; above 3wt%, over 50% of ionomer exist in primary aggregate form.

The third group of ionomer in solution was found to have diameters of over 1000nm, while they are typically around 5000nm. Electrostatic interactions between the non-ionized ion-pairs of primary aggregates are suggested to be the process by which these secondary aggregates are formed [Wu *et al.,* 1996]. Secondary aggregates formed from primary aggregates first appear at approximately at 0.4wt% ionomer concentration. The volume percentage of secondary aggregates ranged from a few percent to 50 volume percent throughout the concentration range examined. The size and volume distributions of these secondary aggregates are shown below:

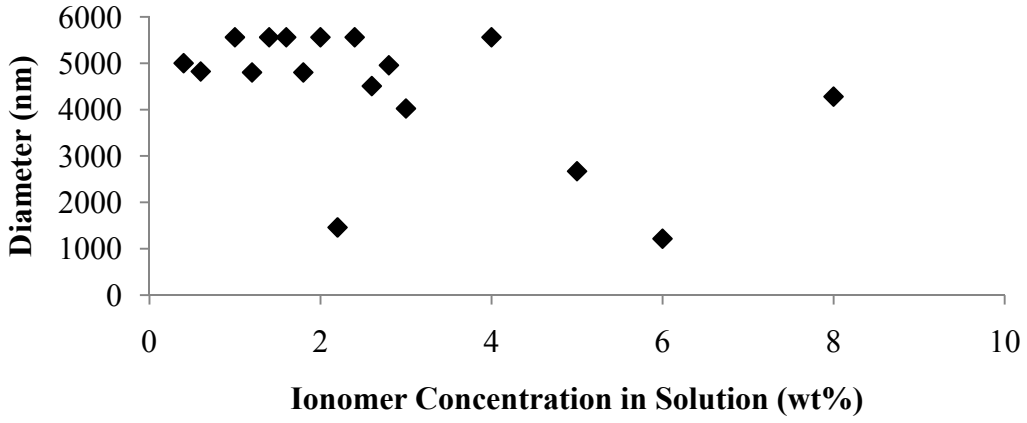

(a)

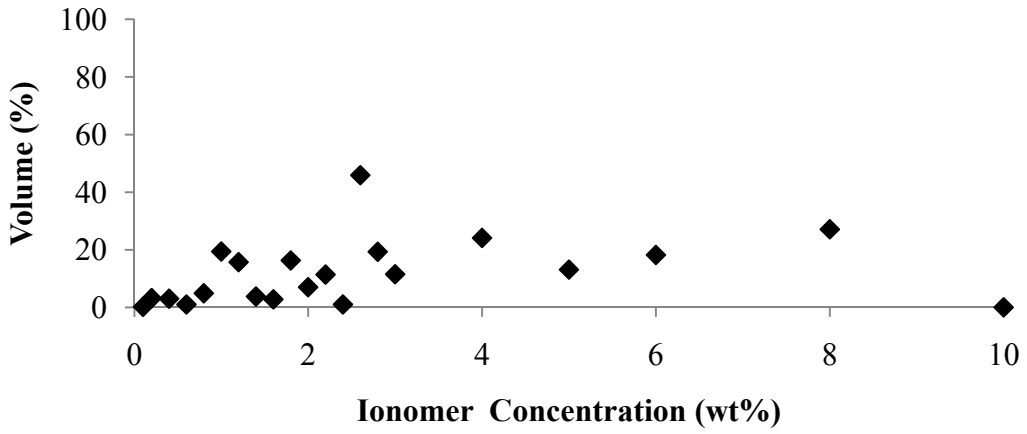

(b)

Figure 4-5 Ionomer secondary aggregates, size and volume distributions. (a) size distribution of ionomer secondary aggregates – Most of the secondary aggregates have diameters between 4000nm and 5500nm; (b) volume distribution of ionomer secondary aggregates.

The zeta potential of the ionomer aggregates in solution was measured by Laser Doppler electrophoresis. Zeta potential values at different concentrations are shown in Figure 4-6 below.

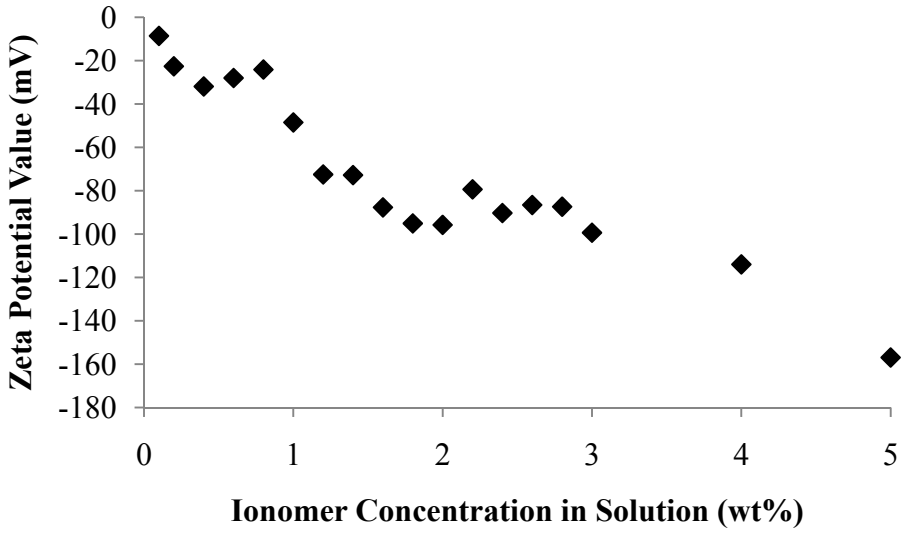

Figure 4-6 Ionomer aggregates, zeta potential values in 1-propanol/water mixture at 1:1 weight ratio.

The pKa value of sulfonate side chain of ionomer was found around -6 [Kreuer, 2001], thus the sulfonic acid groups are fully dissociated in 1-propanol/water mixture and resulted in negatively charged size chain [Pan *et al.,* 2008].

The measured zeta potential value shows variation with concentrations. While the ionomer aggregate volume distribution also varies with concentration, it is possible that the zeta potential value is associated with aggregate size or form. Zhang *et al.,* [2007] suggests that ionomer exist in extended molecular chain have low the charge density along the polymer chain. As concentration increase, ionomer aggregate through hydrophobic interactions of backbone to form primary aggregates. The formed rod-shape

structure of ionomer chains results in higher local charge density than individual chains, and consequently larger zeta potential value. However, in this study, multi-model size distribution exists in most ionomer concentrations. Since zeta potential value only corresponds to mono-model size distribution, it is not clear how zeta potential associated with aggregate size distribution.

4.2 Aggregation Behaviour of Ionomer in Different Solvents

The size distribution of ionomer aggregates in different pure solvents was measured by DLS, as summarized in Figure 4-7 below. The size distribution of aggregates is displayed in three ranges, and the numbers in the table indicate volume percentage per size range.

In the 3-methyl-1-butanol and 1-propanol solutions most ionomer exist in molecular form, making these two solvents the best for ionomer among those examined. Approximately 50 volume percent of ionomer exists in molecular form in the n-butyl acetate, DMSO and isopropanol solutions. The rest exists either in primary aggregates (100-1000nm, DMSO), secondary aggregates (>1000nm, n-butyl acetate), or in a mix of both aggregates (isopropanol). Thus DMSO is a better solvent than isopropanol, and isopropanol is a better solvent than n-butyl acetate. Water and ethylene glycol were

determined to be the two poorest solvents, since ionomer did not completely dissolve in either solvent.

0.1wt% ionomer in 3-methyl-1-butanol, n-butyl acetate, 1-propanol, isopropanol and DMSO yielded clean transparent solutions; turbidity exists in the ionomer/ethylene glycol solution; un-dissolved ionomer film (precipitate) was found in Ionomer/water solution.

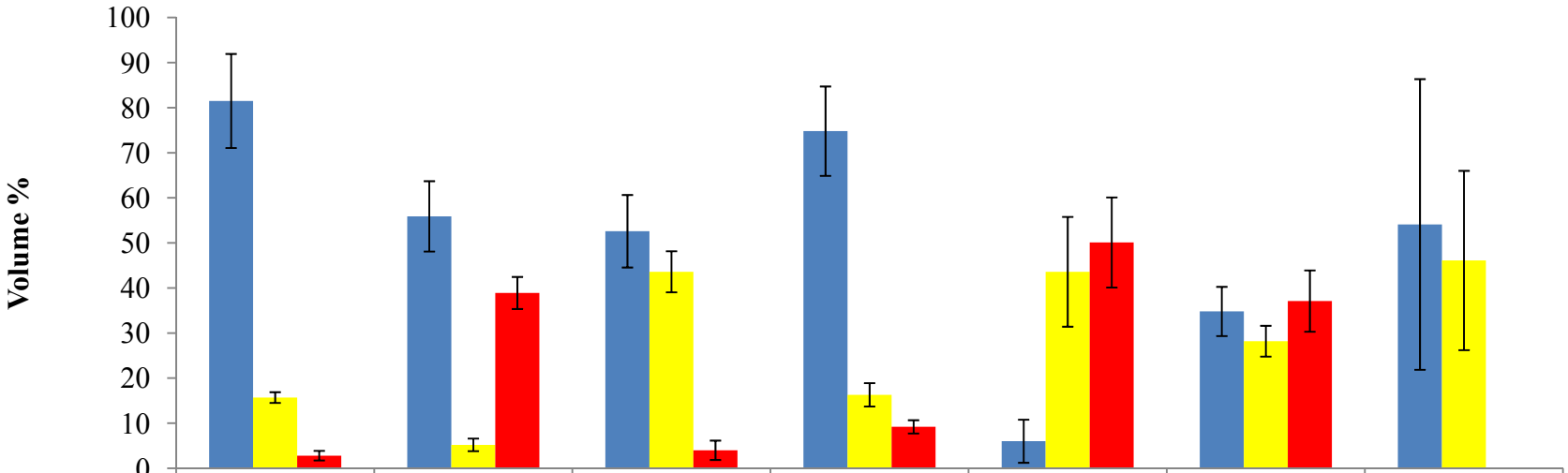

	3-methyl-1-butanol	n-Butyl acetate	DMSO	1-propanol	Water	isopropanol	Ethylene Glycol
0-100nm	81.5	55.9	52.6	74.8	6	34.8	54.1
100-1000nm	15.7	5.2	43.6	16.3	43.6	28.2	46.1
>1000nm	2.8	38.9	4	9.2	50.1	37.1	0

Figure 4-7 Volume aggregate size distribution of 0.1wt% Ionomer solution in different pure solvents. Bars indicate Standard Deviation. The ionomer aggregates are categorized into three groups: the ionomer molecule, with diameter less than 100nm; the primary aggregate, with diameter range from 100nm to 1000nm; the secondary aggregate, with diameter above 1000nm.

It was found that the aggregation of ionomer molecules in solvents is strongly dependent on the solubility parameter of solvents [Ramya et al., 2006]. Yeo *et al* [1980] determined the solubility parameters as 9.5 $(calcm^{-3})^{1/2}$ for ionomer backbone and 16.8 $(calcm^{-3})^{1/2}$ for the side chains. A comparison of the solubility parameters of ionomer and solvent used is shown Table 4-1 below:

Table 4-1 Solubility parameters of ionomer and solvents [Hansen, 2000; Yeo *et al.,* 1980]

	Solubility Parameter $((calcm^{-3})^{1/2})$	
Ionomer	9.5[2] (backbone)	16.8[2] (side chain)
3-methyl-1-butanol	10.4[3]	
n-butyl acetate	8.5[3]	
DMSO	13.0[3]	
1-propanol	12.0[3]	
Water	23.3[3]	
Isopropanol	11.5[3]	
Ethylene glycol	16.1[3]	

The aggregate size distribution of ionomer in solution was found to decrease when the solubility parameter of the solvent was close to the solubility parameter of the ionomer backbone [Ma *et al.,* 2009; Lin *et al.,* 2005]. The solvents 3-methyl-1-butanol, n-butyl acetate, 1-propanol, isopropanol and DMSO are compatible with the perfluorocarbon backbone and not compatible with the side chain. Thus, few aggregates should exist in these solvents.

[2] Solubility parameter obtained from Yeo et al., 1980.
[3] Solubility parameters obtained from Hansen, 2000.

The noncombinatorial free energy of mixing of ionomer's backbone and side chain in each solvent, $\Delta G^{M}_{noncomb}$, is calculated by applying equation 2-28 at 0.1wt% ionomer concentration. The result is shown in below.

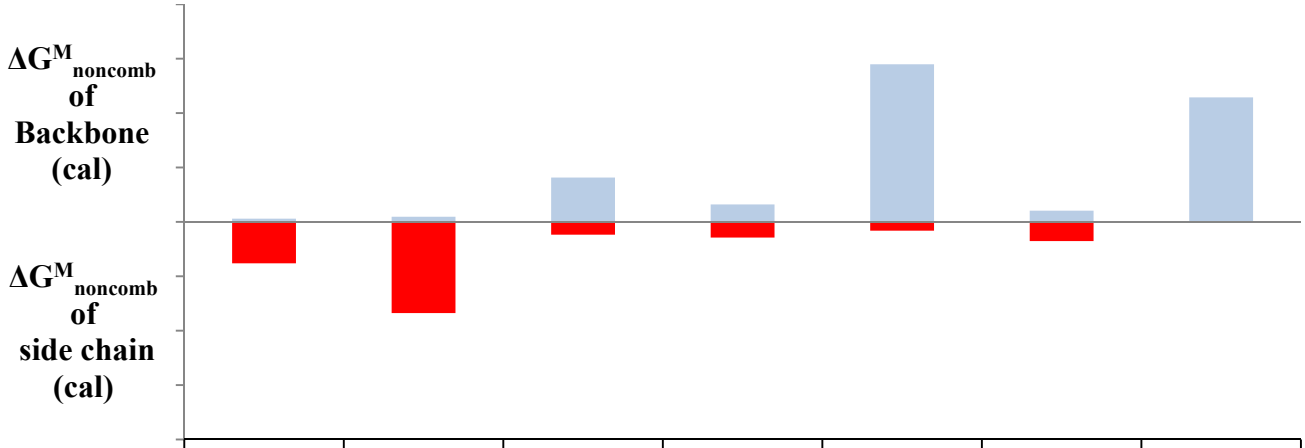

	3-methyl-1-butanol	n-butyl acetate	DMSO	1-propanol	Water	Isopropanol	Ethylene glycol
Backbone	0.030	0.047	0.408	0.161	1.448	0.103	1.145
Side Chain	0.380	0.839	0.118	0.145	0.081	0.176	0.003

Figure 4-8 The noncombinatorial free energy of mixing of ionomer backbone and size chain in each solvent. Ionomer concentration in solution is 0.1wt%. The volume fraction ratio of ionomer backbone to size chain is assumed to be 4:1.

Thermodynamics requires that the free energy of mixing must be zero or negative for solution process to occur spontaneously. Thus, the larger the $\Delta G^{M}_{noncomb}$ value is, the less likely the solution process will occur, and more likely aggregate will form. Comparing with the DLS measurement from figure 4-7, the noncombinary free energy of mixing

shows some correlation with the aggregate size distribution. For example, the large $\Delta G^{M}_{noncomb}$ value for ionomer size chain in n-butyl acetate corresponds to the large volume percent of ionomer secondary aggregate in the solution. Solvents have high $\Delta G^{M}_{noncomb}$ for ionomer backbone, such as DMSO, water and ethylene glycol, comprise larger volume percent of primary aggregate than other ionomer/solvent mixture.

4.3 Aggregation Behaviour of Ionomer in Different Co-Solvent Mixtures

The aggregation behaviour of ionomer in different solvent mixtures at 0.1wt% was measured by DLS. Observations of the bulk solution are recorded in Table 4-2.

Table 4-2 Observation of 0.1wt% ionomer in different solvent mixtures

Ionomer concentration	0.1wt%	0.1wt%	0.1wt%	0.1wt%
Mixing ratio (co-solvent/water)	4:1 wt	2:1wt	1:1wt	1:2wt
1-propanol	clear	clear	clear	clear
isopopanol	clear	clear	clear	clear
DMSO	clear	turbidity	turbidity	turbidity
n-butyl acetate	Immiscible	Immiscible	Immiscible	Immiscible
3-methyl-1-butanol	Immiscible	Immiscible	Immiscible	Immiscible

It is found that 3-methyl-1-butanol and n-butyl acetate are immiscible with water at all mixing ratios. DMSO is miscible with water at all mixing ratios examined; however, turbidity was observed in DMSO/water at 2:1, 1:1 and 1:2 weight ratios when ionomer were present. DLS measurement shows most ionomer exists in primary aggregate form in

DMSO/water at 4:1 ratio. The rest of the 0.1wt% ionomer/solvent mixtures produce clear solutions.

The aggregate size distributions of 0.1wt% ionomer in 1-propanol/water solvent mixtures at weight ratio are shown in Figure 4-7 below, viscosity of 1-propanol/water mixtures was taken from literature [Mikhail, et al., 1963].

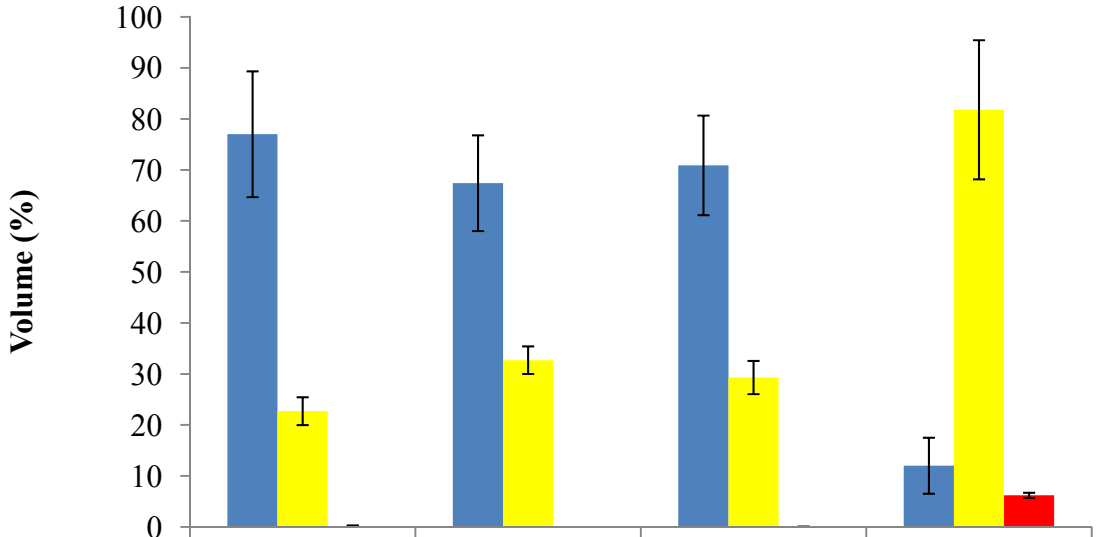

	4:1	2:1	1:1	1:2
0-100nm	77	67.4	70.9	12
100-1000nm	22.7	32.7	29.3	81.8
>1000nm	0.2	0	0	6.2

Figure 4-9 Ionomer aggregates size distribution in volume in 1-propanol/water mixture. Bars are standard deviation. Ionomer concentration in solution is 0.1wt%.

It is observed that when the 1-propanol-to-water ratio is greater than 1, most ionomer exists in molecular form. When the 1-propanol-to-water ratio is below 1, most ionomer transform into primary aggregates.

Aggregate size distribution of 0.1wt% ionomer in isopropanol/water solvent mixtures at different concentrations is shown in Figure 4-8 below, viscosity of isopropanol/water mixture was taken from literature [Herráez et al., 2004].

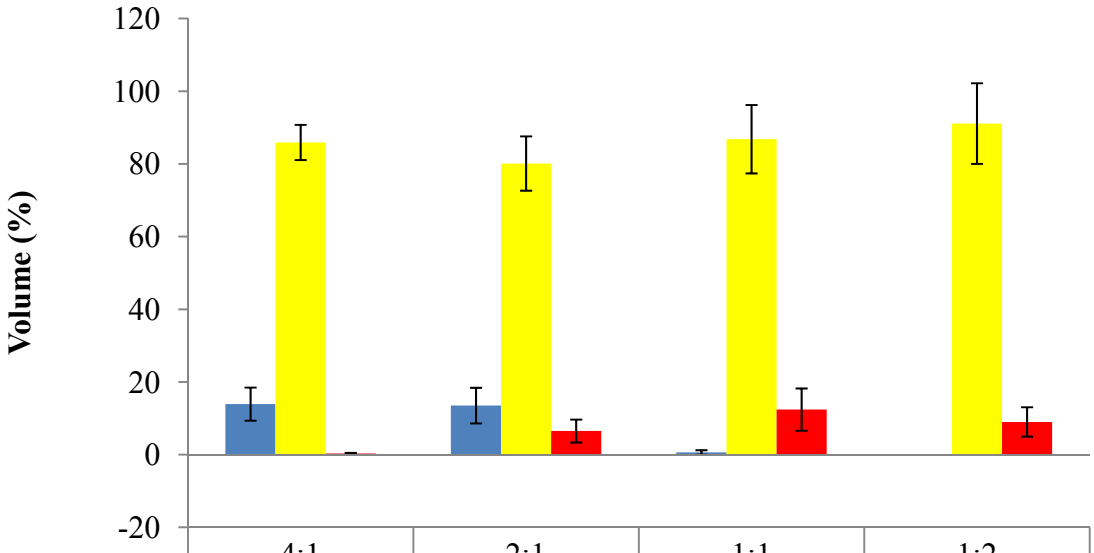

	4:1	2:1	1:1	1:2
0-100nm	13.9	13.5	0.6	0
100-1000nm	85.9	80.1	86.8	91.1
>1000nm	0.3	6.5	12.4	9

Figure 4-10 Ionomer aggregates, size distribution with standard deviation in isopropanol/water mixture. Ionomer concentration in solution is 0.1wt%.

It is observed that most ionomer exist in primary aggregate form in all solvent mixing ratios. The molecular form of ionomer exists at isopropanol-to-water ratios greater than 1, and disappears at isopropanol to water ratios of less than 1. Secondary aggregates appear in isopropanol/water at 1:1 and 1:2 wt ratios.

4.4 Summary

The aggregation behaviour of ionomer was investigated by Dynamic Light Scattering under various conditions. The influence of concentration on the aggregate size distribution of ionomer in 1-propanol/water solvent mixture was investigated from 0.1wt% to 10wt% ionomer concentration. Most ionomer exist in molecular chains in solutions between 0.1wt% and 3wt%. From 3wt% to 5wt%, the primary aggregation process occurs and most ionomer molecular chains aggregate into primary aggregates. At above 5wt% ionomer concentration, most ionomer exist in primary aggregate form. The measurement of zeta potential also validates the aggregation process, where a rapid drop of zeta potential values occurs at onset of aggregate formation. At 0.4wt%, where secondary aggregates appear, the first rapid decrease in zeta potential occurs. At 3wt%, where most ionomer molecular chains aggregate into primary aggregate form, another drop in zeta potential is observed.

The solubility of ionomer in different solvents was investigated and the aggregate size distribution of 0.1wt% ionomer in these solvents was measured. Results show that 3-methyl-1-butanol and 1-propanol are the two best solvents for dissolving ionomer since most ionomer exist as molecular chains in these two solvents. DMSO, n-butyl acetate and isopropanol are only moderately effective solvents for dissolving ionomer, as only approximately 50 volume percent of ionomer dissolved into molecular form. Water and ethylene glycol are poor solvents, since crystalline turbidity/un-dissolved ionomer were found in these two solvents.

The size distribution of ionomer aggregates in different solvent compositions was investigated at four solvent/water ratios for 3-methyl-1-butanol, n-butyl acetate, DMSO, 1-propanol and isopropanol. 3-methyl-1-butanol and n-butyl acetate were found to be immiscible with water at all mixing ratios before dissolving ionomer films. Ionomer were found to be partial/non soluble in the DMSO/water solvent mixture below a 4:1 DMSO to water ratio. When mixed with water, 1-propanol was found to be a better co-solvent than isopropanol at all mixing ratios.

Stage 1 has found that, among the solvents examined, 1-propanol is the best solvent to dissolve ionomer, both as a pure solvent and in mixtures with water. Thus, 1-propanol

will be the co-solvent of choice in subsequent investigations involving water/co-solvent mixtures.

Chapter 5

Aggregation Behaviour of Carbon Black Dispersion

The results of an investigation on the aggregation behaviour of Carbon Black (Vulcan XC72) in solution are presented in this chapter. The effects of sonication time, CB concentration and solvent type/composition on the particle size distribution of CB were examined by Dynamic Light Scattering. The particle size distributions of CB (Vulcan XC72) and 10wt% Pt/CB were also compared.

5.1 The influence of sonication time on Carbon Black Particle Size Distribution

Sonication is a common method used to disperse carbon black in solvent. The effects of sonication time on the particle size distribution of carbon black in 1-propanol, isopropanol and DMSO were explored. 0.01wt% CB dispersion prepared from these solvents were sonicated continuously for 12hrs. The particle size distributions of the CB were measured after 0.5hr, 1hr, 2hrs, 4hrs, 8hrs and 12hrs of sonication. The results are shown in Figure 5-1 below.

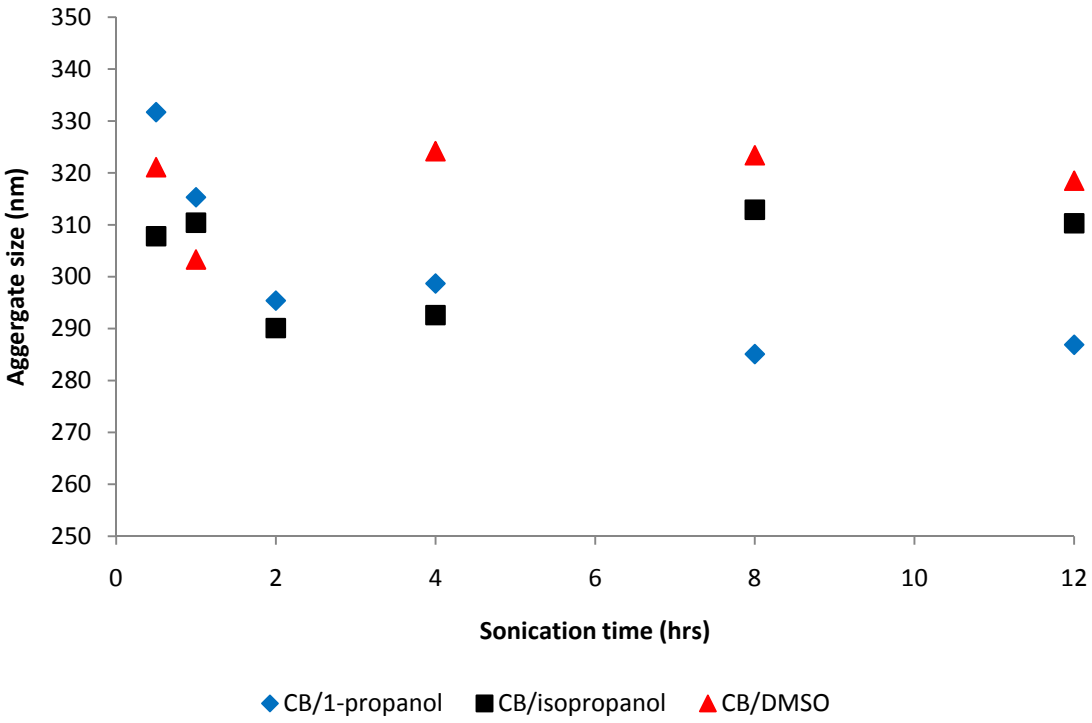

Figure 5-1 Particle size distributions of 0.01wt% CB dispersions in varying period of sonication; solvents are 1-propanol, isopropanol and DMSO.

The trend of CB particle size distribution change in varying period of sonication is not clear. In CB/1-propanol and CB/DMSO solutions, the particle size decreased approximately 20nm after 0.5hr to 1hr of sonication. In the CB/isopropanol solution, the particle size decreased approximately 20nm after 1hr to 2hrs of sonication time. Although initial sonication (0.5hrs to 2hrs) seems to reduce the particle diameter, further sonication does not improve the size distribution. All three CB dispersions showed no significant

change in particle size distribution of CB after 2hrs of sonication. The CB particle size was found around 310nm in the sonication length examined. The effect of solvent on the size distribution of CB particle is not significant as the size difference in these solvents is relatively small (40nm or less). All three solvents are equally good for dispersing CB. For the purpose of preventing platinum removal from CB surface, 0.5hr of sonication is suggested.

5.2 Carbon Black Particle Size Distribution in Solution at Different Concentrations

The concentration effect on CB particle size distribution was examined from 0.0001wt% to 1wt% CB concentration in 1-propanol, isopropanol and DMSO solutions. The results are shown in Figure 5-2.

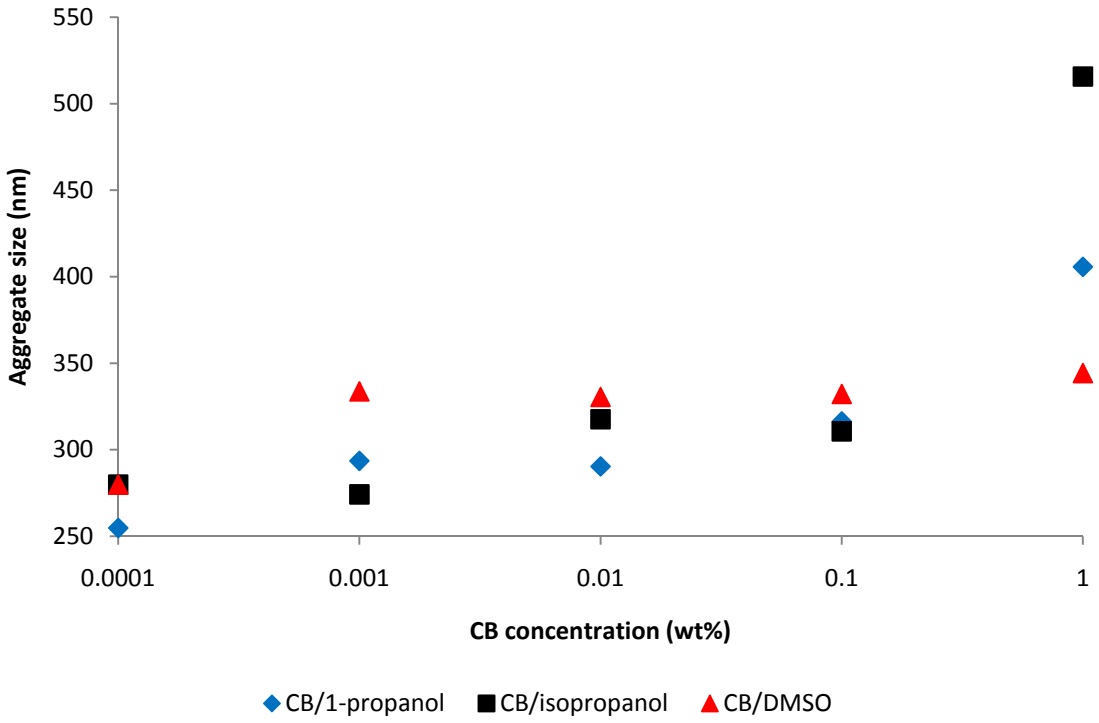

Figure 5-2 CB particle size distribution at different concentrations; solvents are 1-propanol, isopropanol and DMSO; samples were sonicated for 2hrs before measurement.

The CB particle size distribution increased with increasing concentration. However, due to the limitation of the DLS technique, at higher sample concentration, the measured particle size will be smaller than the real size because of the multiple scattering phenomena, the measured particle size distributions for CB from 0.1wt% and above is smaller than the actual particle size distributions in the solution. Between 0.0001wt% to 0.01wt%, particle size distributions of CB in 1-propanol vary from 250nm to 300nm,

while in isopropanol and DMSO the particle size distributions vary from 275nm to 325nm. An average particle size increase of 50mn is seen in all three solvents from 0.0001wt% to 0.01wt%.

The aggregation behaviour of CB in 1-propanol/water co-solvent mixtures at different mixing ratios was also investigated. Particle size distributions and zeta potential values of 0.01wt% of CB in 1-propanol/water mixture were measured (Figure 5-3). The size of CB aggregates in 1-propanol/water mixture varies with water content in the solvent mixture. CB aggregates with a single model size distribution and a mean diameter of approximately 300nm were found in 1-propanol/water mixture at 4:1, 2:1 and 1:1 weight ratios. In a CB/1-propanol/water solution at 1:2 1-propanol to water ratio, there exist two size distributions: approximately 70 volume% of CB aggregates exist in the first model, with a mean diameter of around 300nm, and approximately 30 volume% of CB aggregates exist in the second model, with a mean diameter of approximately 700nm. The zeta potential values drop as water content in the solvent mixture rises from 20wt% to 50wt%, but increases when water content increases from 50wt% to around 66wt%.

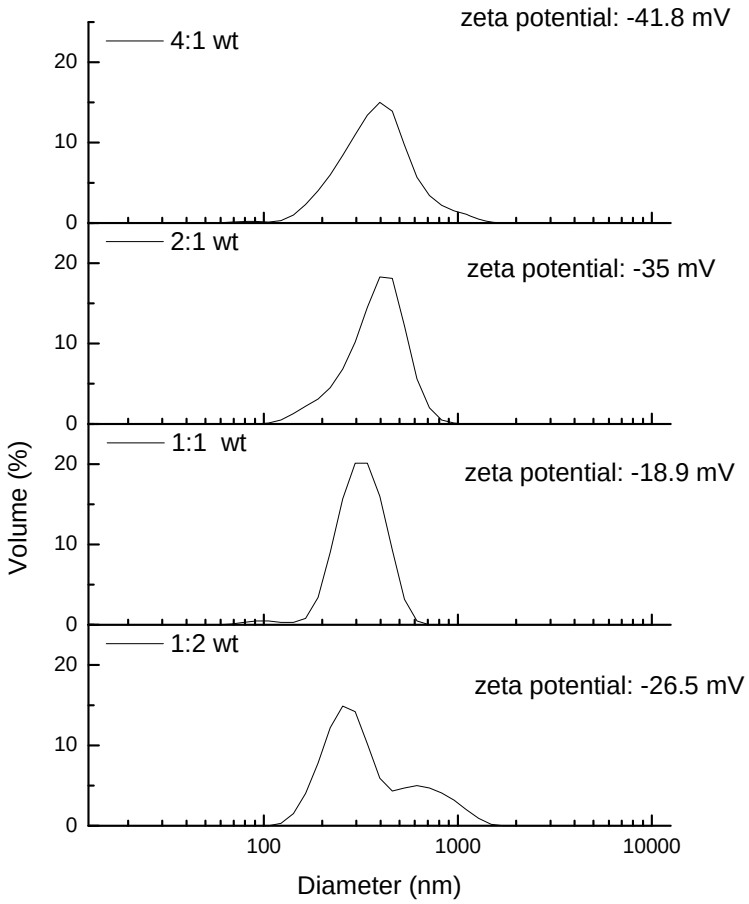

Figure 5-3 Particle size distributions and zeta potential values of CB in 1-propanol/water mixture; CB concentration is 0.01wt% and solvent mixing ratio is 4:1, 2:1, 1:1 and 1:2 1-propanol to water in weight.

The change in the zeta potential value and size distribution can be explained by Lewis acidity and basicity of CB and pure solvents. In a suspension with no additional ionic

species, the charges on the slipping plane of CB particles, which determine the zeta potential value, come from either ionization of surface groups, or electron transfer from the medium [Van Der Hoeven, *et al.,* 1992]. If the particles react as Lewis acids to the medium, they will attract electrons from the medium and result in higher zeta potential values; conversely, if particles react as Lewis bases to the medium, they will donate electrons to the medium, resulting in lower zeta potential values.

When dispersed in media except water, where each molecule contains only one oxygen atom, CB behaves as a Lewis acid receiving electron pairs, and showing negative zeta potential; in water CB behave as a Lewis base donating electron pairs and showing positive zeta potential [Xu, *et al.*, 2007]. Thus, when the water content in the solvent mixture increases, fewer electrons are attracted to the slipping plane, resulting in a drop in the zeta potential value. When water content in the solvent mixture increases above 50wt%, the zeta potential of the aggregates is not strong enough to repel CB particles, aggregation process occurs, and a second aggregate size distribution with a greater diameter is formed.

5.3 Particle Size Distribution of Pt/CB vs CB in Solution

The particle size distributions of Vulcan XC-72 Carbon Black and 10wt% Pt on Vulcan XC-72 Carbon Black (ETEK Inc., MA, USA) were compared in this study. The presence of Pt particles on the CB surface was found to have no significant influence on particle size distribution. The measured result is shown in Figure 5-4 below:

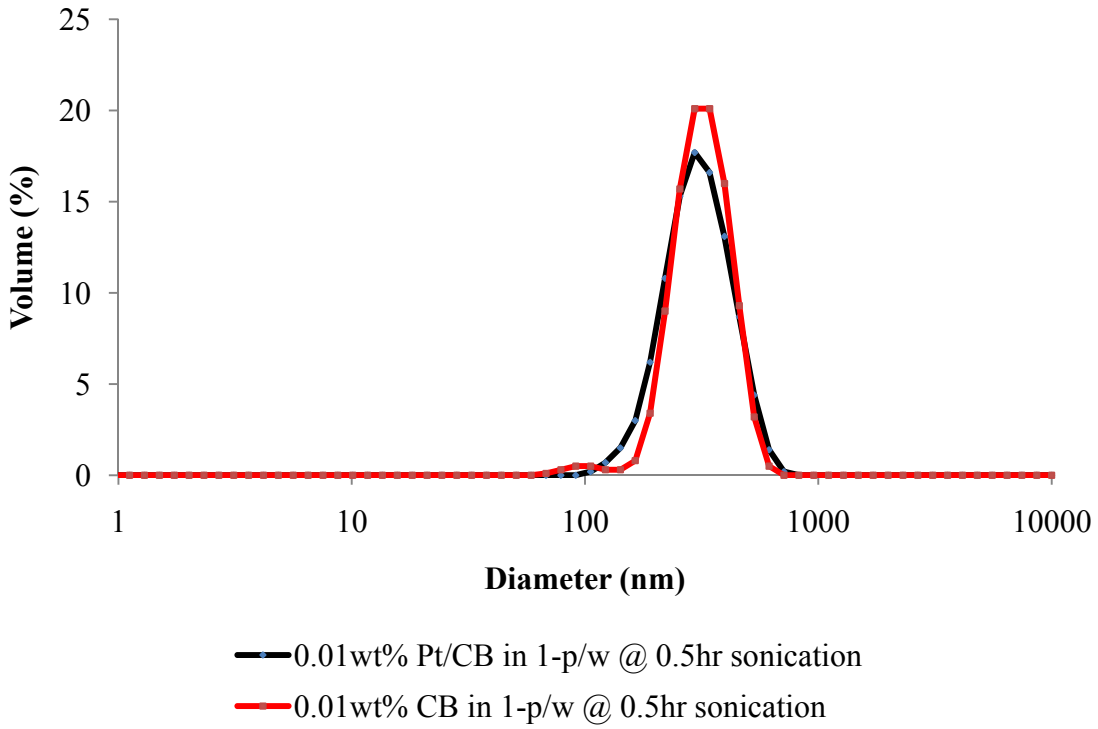

Figure 5-4 Particle size distribution of CB and Pt/CB in solution, CB and Pt/CB concentration are 0.01wt%; the solvent is a 1-propanol/water mixture at 1:1 weight ratio. Samples were sonicated for 0.5hr before measurement.

Both 0.01wt% dispersion of CB and Pt/CB (10wt% Pt)in 1-propanol/water at 1:1 wt ratio have a mean size distribution of 300nm, and Pt/CB has a slightly narrower distribution than CB. This investigation suggests that the particle size distribution of CB and Pt/CB should be similar, thus the measured CB aggregation behaviour should be very close to (but not exactly) that of Pt/CB in solution.

5.4 Summary

The investigation of the effect of sonication time, CB concentration and solvent composition on the particle size distribution of CB in solution revealed that CB aggregate size does not change significantly after 2 hours of sonication in the solvents selected. The increment in particle size distribution from 0.0001wt% to 0.01wt% is approximately 50nm for all solvents examined. Particle size readings beyond 0.1wt% were not reliable due to the limitations of the measuring instrument. Aggregation behaviours of CB in 1-propanol/water solvent mixture at different mixing ratios were also investigated. The CB particle size distribution was strongly correlated to the water content in the solvent mixture. Aggregate size distribution was found to be around 300nm for solutions in which the water content in the solvent mixture was 20wt%, 33wt% and 50wt%. When water content was above 50wt%, the particle size of CB shifted significantly resulting in the formation of aggregates at greater diameters.

The water content in the solvent mixture is an important parameter affecting the size of CB aggregates in solution at the CB concentration levels examined. When water content was below 50wt% in the solvent mixture, the aggregate size did not vary with changes in water content. However, once water content reached above 50wt%, the aggregate size distribution changed and bigger aggregates formed from the aggregation process.

Chapter 6

Interactions Between Pt/CB and Ionomer

The observations and results presented in this chapter are from investigations of the interactions between Pt/CB and ionomer in dispersion. The adsorption of ionomer on the Pt/CB surface and the hydrodynamic size changes of the aggregates resulting from the adsorption of ionomer on Pt/CB were examined by ^{19}F NMR and Dynamic Light Scattering. The geometry of ionomer molecules in solution was also estimated to aid in understanding the adsorption.

6.1 Adsorption of Ionomer on Pt/CB

The adsorption of ionomer on the catalyst material during the preparation process of the catalyst layer of PEM fuel cells will affect the structure of the catalyst layer and, therefore, the performance of the PEM fuel cell [Komoda *et al.,* 2009]. Understanding the adsorption characteristic of ionomer on the platinum support can provide valuable insight on the electrochemical performance of PEM fuel cells.

A NMR spectrum of ionomer solution with respect to $CFCl_3$ is shown in Figure 6-1, together with the chemical shifts (in ppm) and group assignments.

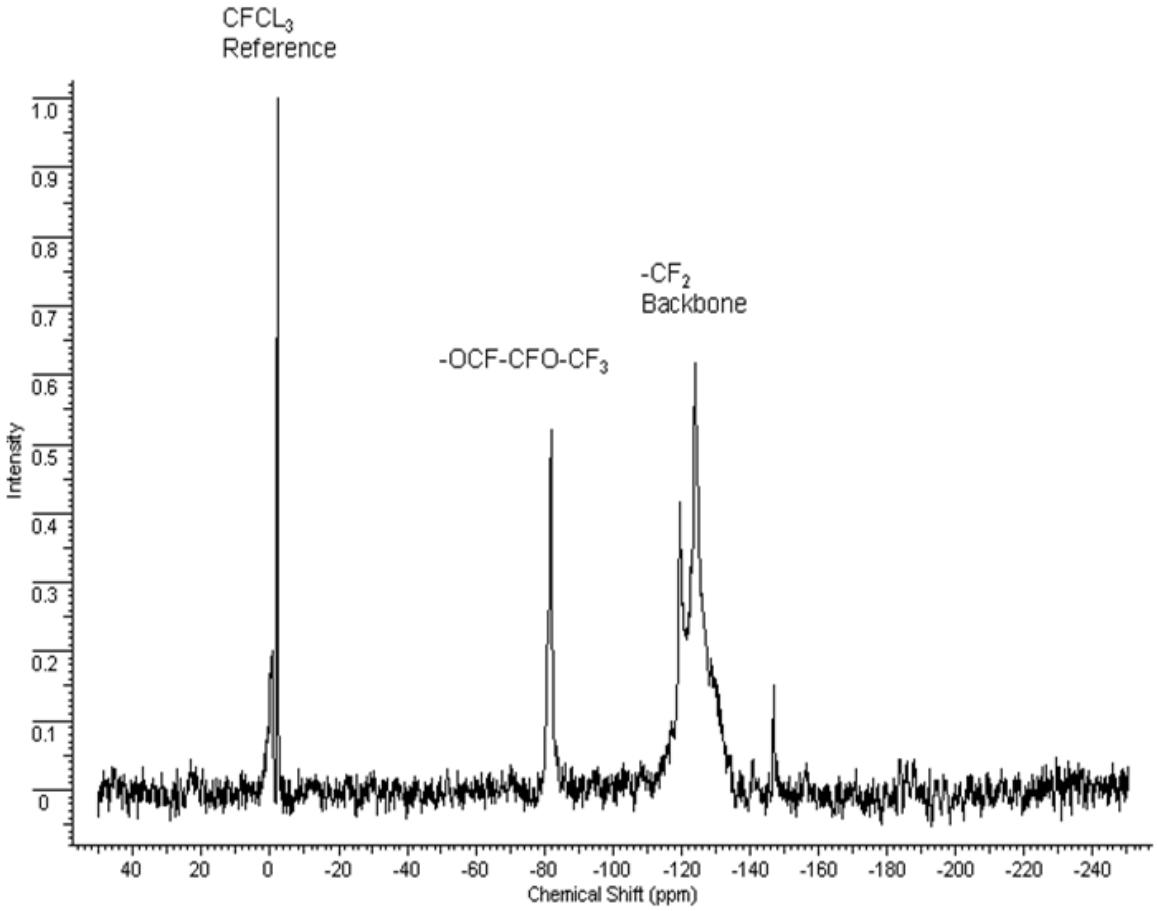

Figure 6-1 ^{19}F NMR spectrum of ionomer and reference after phase and baseline correction.

The peak at 0 ppm corresponds to the reference material, trichlorofluoromethane. The strongest peak, at -120 ppm, is due to ^{19}F nuclei in $–CF_2$ groups in the ionomer backbone; the peak at -80 ppm is due to the OCF_2 group near the carboxylic group and in the repeat

unit; the weak peak at about -146 ppm is due to ^{19}F nuclei in the CF groups [Schilick *et al.,* 1991].

The reference and ionomer backbone signals were used in the study. A series of ionomer solutions were measured with ^{19}F NMR with same reference, and the intensity ratios between ionomer backbone and reference were correlated with ionomer concentration. A standard curve is shown in figure 6-2 below:

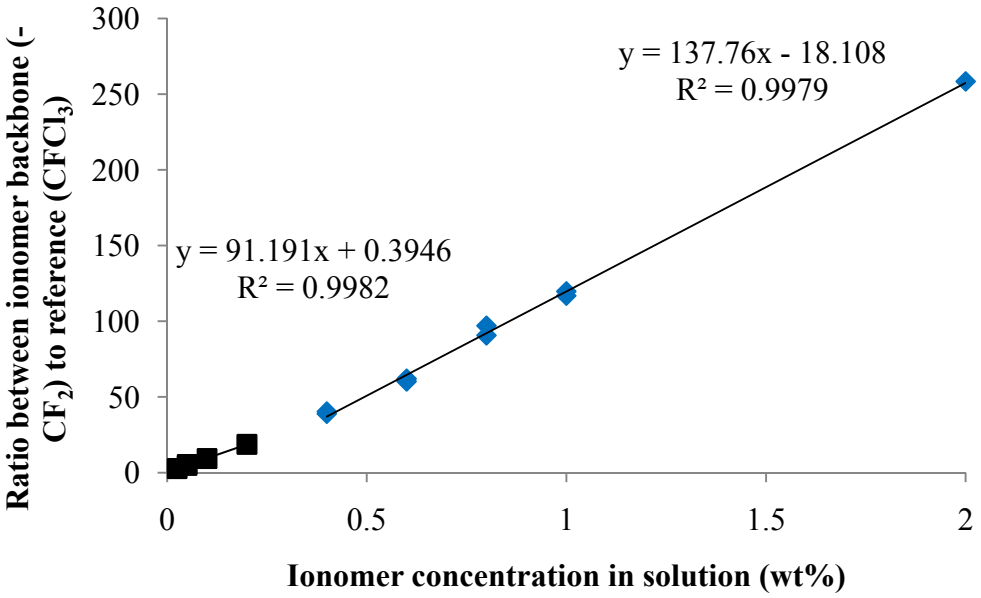

Figure 6-2 Calibration curves with R^2 values of ionomer in 1-propanol/water solution.

The data was fitted into two separate curves to achieve best fitting: data between ionomer concentrations of 0 to 0.2wt% were fitted into y=91.191x+0.3946 and data between 0.4 to 2wt% were fitted into y=137.76x-18.108.

Thus, the linear functions of the NMR signal ratio and ionomer concentration are:

$$\frac{S_{-CF_2}}{S_{CFCl_3}} = \mathbf{0.3946} + \mathbf{91.191} \times \boldsymbol{C_{ionomer}},\ \ \mathbf{0} < \boldsymbol{C_{ionomer}} \leq \mathbf{0.2} \tag{6-1}$$

$$\frac{S_{-CF_2}}{S_{CFCl_3}} = -\mathbf{18.108} + \mathbf{137.76} \times \boldsymbol{C_{ionomer}},\ \ \mathbf{0.4} \leq \boldsymbol{C_{ionomer}} \leq \mathbf{2} \tag{6-2}$$

The above two equations were used to calculate the supernatant ionomer concentrations. Once the equilibrium ionomer concentrations were calculated, the amount of ionomer adsorbed on the Pt/CB surface could also be calculated. An adsorption isotherm was constructed based on the ionomer equilibrium concentration and the ratio of ionomer adsorbed on the Pt/CB surface, shown on the graph below. The unit surface area of 10wt% Pt/CB was measured to be 167m^2/g by BET nitrogen adsorption and desorption.

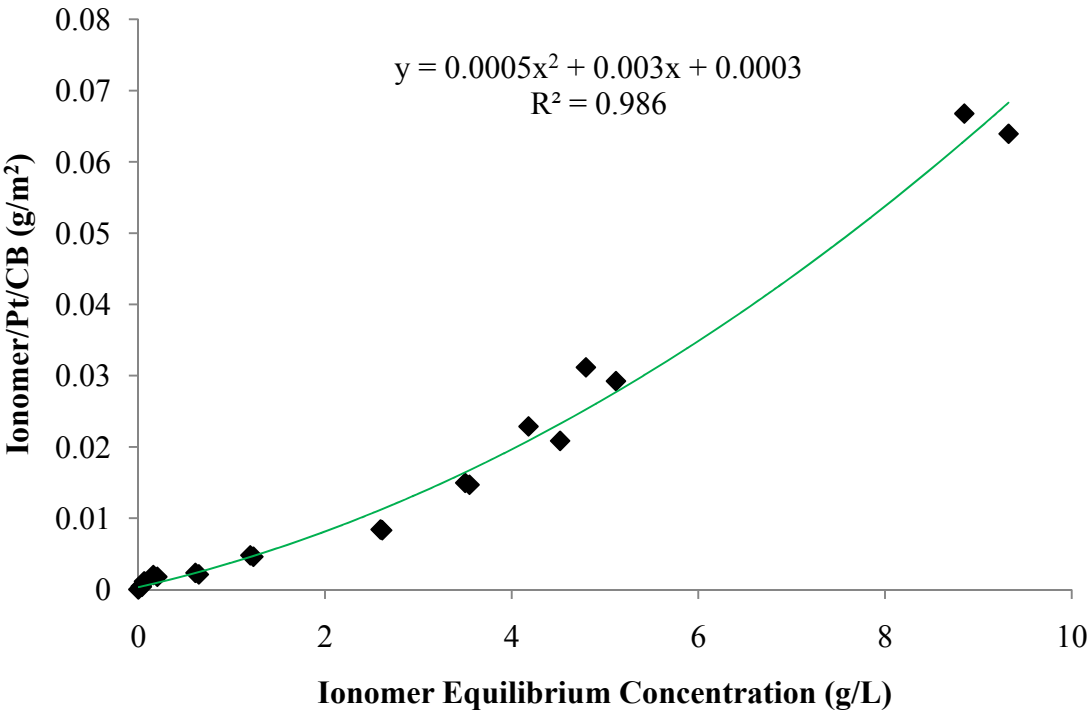

Figure 6-3 Adsorption of ionomer on Pt/CB in 1-propanol/water solution. The solid line is a polynomial (power =2) fitting of the adsorption data; the equation and R^2 value are displayed.

The adsorption of ionomer on the Pt/CB surface exhibits a polynomial growth with increasing ionomer concentration. However, the fitting at low ionomer equilibrium concentration is not precise. A close look at low ionomer equilibrium concentration is shown in Figure 6-4. The Langmuir isotherm [Sohn *et al.,* 2005] was applied to fit the

adsorption isotherm. The dynamic equilibrium between adsorption and desorption of ionomer on the Pt/CB surface can be expressed as follows:

$$\boldsymbol{X_{ionomer} + M_{\frac{Pt}{CB}surface} \overset{k_a k_d}{\longleftrightarrow} XM_{adsorption}} \tag{6-3}$$

where k_a is the adsorption constant and k_d is the desorption constant. Surface coverage (θ_c) is defined as the ratio of the number of adsorption sites occupied to total available sites (N). The rate of change of surface coverage ($d\theta_c/dt$) due to adsorption, depending on the concentration of ionomer (C) and the surface coverage is:

$$\boldsymbol{\frac{d\theta_c}{dt} = k_a CN(1 - \theta_c)} \tag{6-4}$$

The rate of change of θ_c due to desorption is proportional to the number of adsorbed ionomer, $N\theta_c$, is expressed as:

$$\boldsymbol{\frac{d\theta_c}{dt} = -k_d N\theta_c} \tag{6-5}$$

At equilibrium, the rate of adsorption and desorption is equal, thus solving the above equations yielding the Langmuir isotherm:

$$\boldsymbol{\theta_c = \frac{\Gamma_{eq}}{\Gamma_{max}} = \frac{K_{eq}C_{eq}}{1+K_{eq}C_{eq}}} \tag{6-6}$$

where K_{eq} is the adsorption equilibrium constant ($\frac{k_a}{k_d}$), C_{eq} is the equilibrium ionomer concentration in solution, and Γ_{eq} and Γ_{max} are the equilibrium and maximum surface coverage. The Langmuir equation is often written as:

$$\boldsymbol{d \cdot \theta_c = \frac{(d/b)C}{(d/b)C+1}} \tag{6-7}$$

Where *d* and *d/b* are empirical constant [Hiemenz *et al.,* 1997]. By re-arranging equation 6-7 into the form:

$$\boldsymbol{\frac{C}{\theta_c} = dC + b} \tag{6-8}$$

This form suggests that a plot of *C/θc* versus *C* will be a straight line if the system conforms to the Langmuir isotherm. A plot of *C/θc* versus *C* is shown in Figure 6-4 (a).

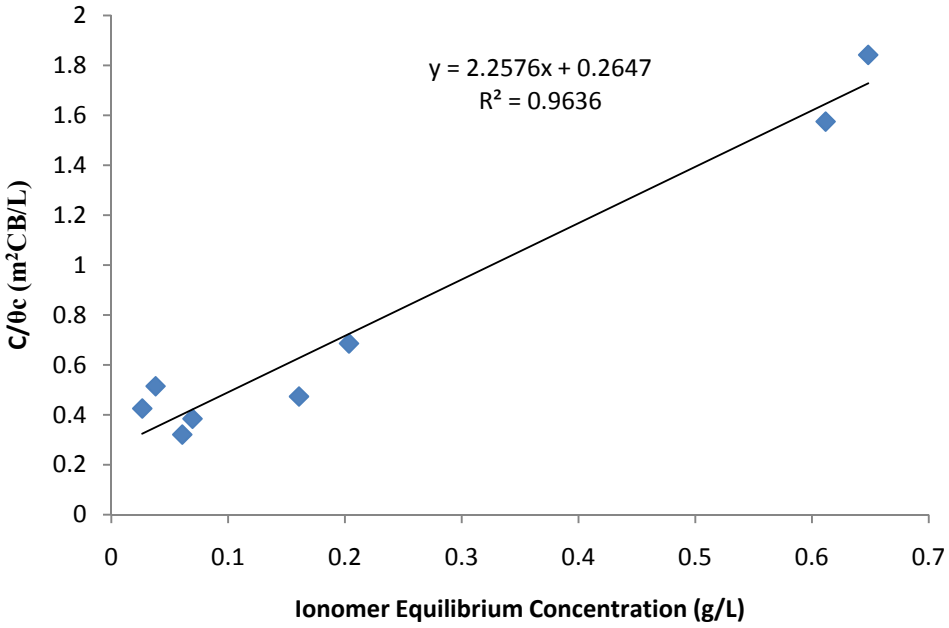

(a)

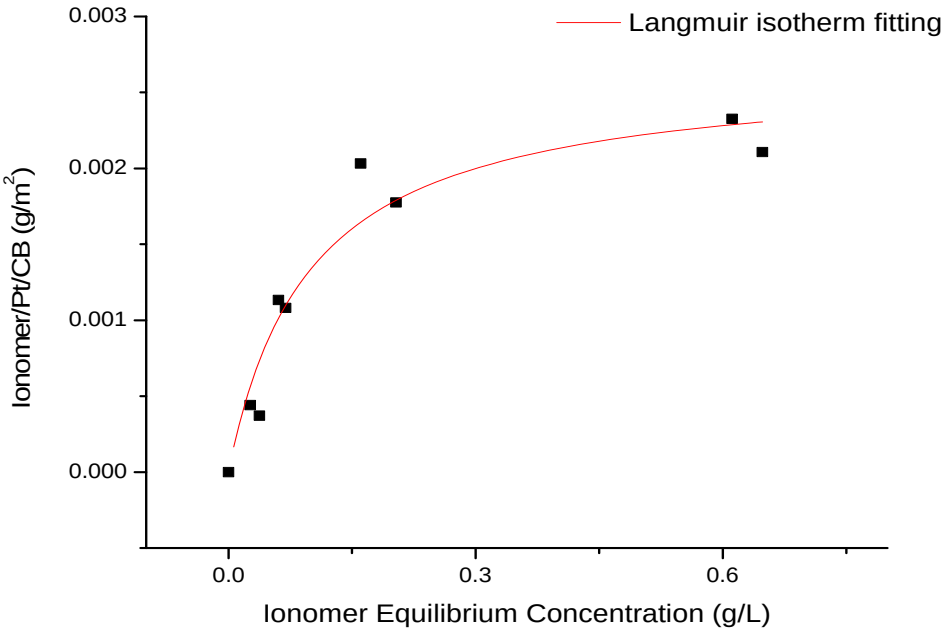

(b)

Figure 6-4 (a) plot of $C/\theta c$ versus C with linear fitting and R^2 value. (b) Ionomer adsorption data with Langmuir isotherm validation and fitting. The line is the Langmuir fitting, plotted using OriginLab 8.0, after converting equation 6-6 into: $\boldsymbol{\Gamma_{eq} = \frac{\Gamma_{max} K_{eq} C_{eq}}{1 + K_{eq} C_{eq}}}$.

The plot of $C/\theta c$ versus C in figure 6-4 (a) shows a linear trend, indicating the adsorption isotherm conforms to the Langmuir isotherm. As shown in Figure 6-4 (b), at low concentrations, ionomer adsorption on the Pt/CB surface was found to follow a Langmuir isotherm; at high concentrations, additional adsorption was also observed. The adsorption

behaviour can be classified into two adsorption processes: primary adsorption starts from zero and progresses to a certain concentration until it reaches a plateau; It is believed that primary adsorption is ionomer adsorbed on the outer surface, and secondary adsorption is ionomer adsorbed in the nanopores of the Pt/CB particle, or formation of a multilayer [Ma *et al.,* 2007]. The adsorption equilibrium constant (K_{eq}) and maximum surface coverage (Γ_{max}) of the primary adsorption were determined and compared to results of similar studies by Ma *et al.,* [2007].

Table 6-1 Parameters summary for Langmuir isotherm of experimental and literature data.

	Maximum surface coverage Γ_{max} (g ionomer/g adsorbate)	Maximum surface coverage Γ_{max} (g ionomer/m^2 adsorbate)	Equilibrium Constant K_{eq}	C_{eq} for secondary adsorption (g/L)
Hispec 9000[4]	0.133	0.00113	13.1	1.05
10wt% Pt/CB[5]	0.444	0.00227	10.2	0.65

The Hispec 9000 Pt/CB samples (57.84wt% Pt/CB) were found to have much higher catalyst loading than the E-TEK samples (10wt% Pt/CB), which indicates that more of the carbon surface area is covered by platinum than that of the E-TEK sample. Compared to the E-TEK sample, smaller maximum surface coverage Γ_{max} values were found for the

[4] Supplier: Johnson Matthey Fuel Cells; 57.84wt% Pt/CB; Carbon support: Vulcan XC 72; BET area: 100m^2/g. [Ma *et al.,* 2007]
[5] Supplier: E-TEK Inc., MA, USA; 10wt% Pt/CB; Carbon support: Vulcan XC 72; BET area: 167m^2/g

Hispec 9000 sample. The phenomenon of decreasing maximum surface coverage as catalyst content increases suggests primary adsorption mainly occurred on the supporting carbon surface rather than on the Pt surface.

6.2 Aggregate Size Change of Pt/CB

Ionomer adsorbed on the Pt/CB surface in solution results in changes to the hydrodynamic radius of the aggregates, causing the diffusivity of the aggregates to change,. An illustration of changes to hydrodynamic diameter caused by the adsorption of ionomer is shown below:

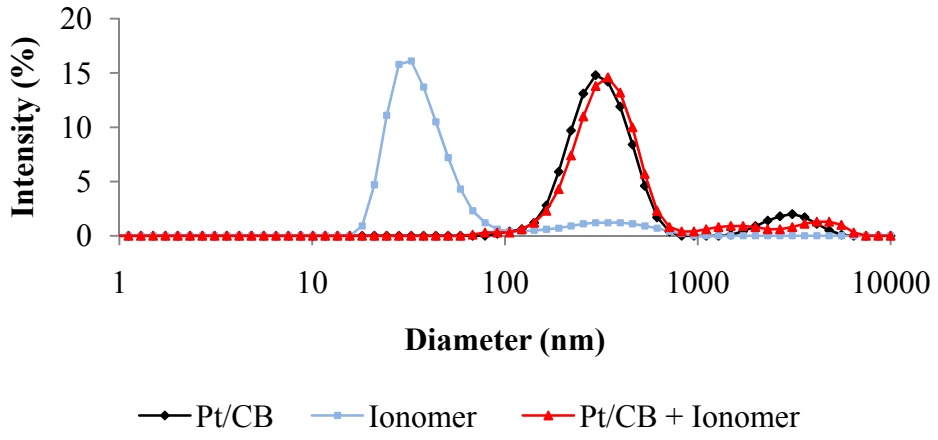

Figure 6-5 Aggregate size distributions of 0.01wt% ionomer, Pt/CB and ionomer/Pt/CB mixture in 1-propanol/water solution.

As shown in Figure 6-5, the aggregate diameter of ionomer+Pt/CB in solution is greater than Pt/CB alone, and the diameter difference between these two samples is close to the hydrodynamic radius of the ionomer added. This indicates that the increment in hydrodynamic size could be a result of ionomer adsorbed on Pt/CB surface. The samples used in the adsorption isotherm were diluted 100 times, while the ionomer equilibrium concentration in the solution was kept constant. Aggregate size distributions of the diluted samples were compared with the Pt/CB particle size distributions and the differences were plotted with the ionomer equilibrium concentration. The result is shown in Figure 6-6:

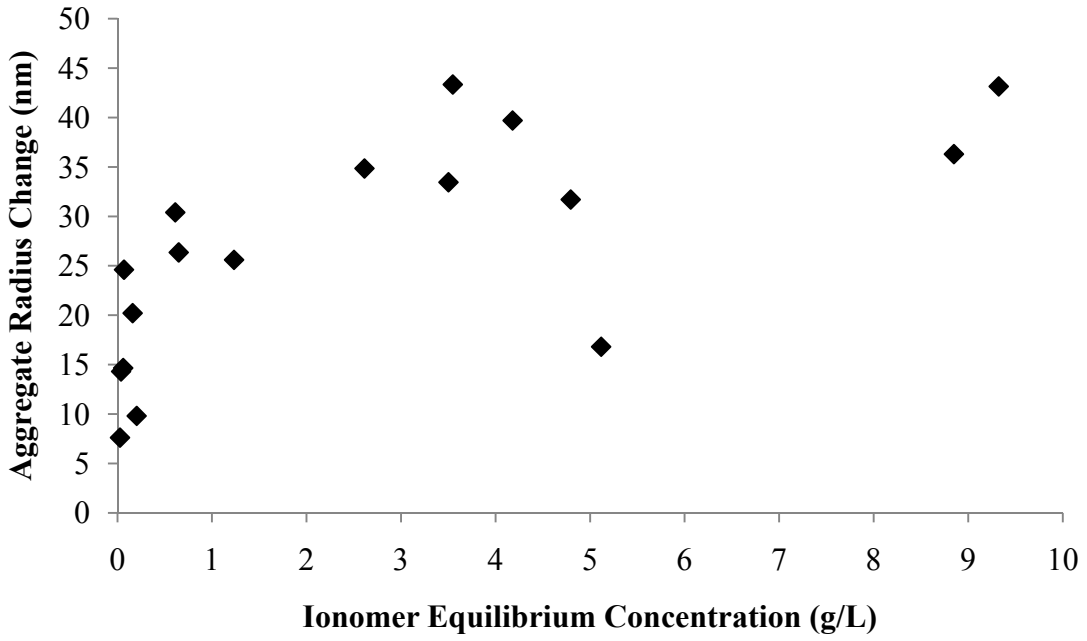

Figure 6-6 Aggregate size differences of Pt/CB and ionomer/Pt/CB solution due to ionomer adsorption. The differenc is calculated as $\Delta R = R_{ionomer/Pt/CB} - R_{Pt/CB}$

The aggregate size difference (ΔR) increases at low ionomer equilibrium concentrations, and reaches a plateau around 40nm at higher concentrations. Compared to the adsorption isotherm, the primary adsorption plateau reached ionomer equilibrium concentration at around 0.65g/L; at this concentration, the ΔR is around 30nm. Secondary adsorption occurred between 0.65g/L and 10g/L, while the ΔR value increased from 30nm to 40nm. Since ionomer have a stronger affinity to carbon than to Pt, the ΔR value from 0nm to 30nm should be the result of ionomer adsorption on carbon surface of the Pt/CB particle. The further increase of the ΔR value from 30nm to 40nm could be the secondary adsorption of ionomer on the Pt surface, the interaction with adsorbed ionomer, or the impregnating of the nanopores by Pt/CB particles. Considering the small increase in ΔR value over a wide ionomer equilibrium concentration range (0.65g/L to 10g/L), most ionomer should be absorbed into the nanopores of Pt/CB particles, or achieved a tighter packing arrangement on the CB surface.

6.3 Ionomer Geometry and Surface Coverage

The surface coverage of ionomer on Pt/CB (m^2 ionomer / m^2 Pt/CB) was estimated under different ionomer geometry assumptions/estimations and binding orientations. Two extreme scenarios were proposed to estimate/measure the unit surface area of Pt/CB particle. CB particle in solution is aggregate consist of smaller sphere particles with diameter around 20nm [Xu, *et al.*, 2007]. The first scenario assumes ionomer molecule

only adsorbed on the external surface area of CB particle, in which the CB particle is assumed as a sphere, the average diameter measured from DLS is around 300nm, leading to a unit surface area of 12.4m^2/g, referred as DLS area. This assumption yields the minimal available adsorption surface for ionomer. If assuming ionomer adsorbed on specific (total) area, considered as an irregular particle, the unit surface area is measured by BET nitrogen adsorption-desorption to be 167m^2/g, referred as BET area. This assumption yields maximal available adsorption surface for ionomer. Two ionomer geometries were considered when estimating the surface coverage (m^2 ionomer/m^2 Pt/CB) of ionomer on Pt/CB surface: a sphere or a rod shaped particle. When consider ionomer as rod shaped particle, two extreme adsorption configuration was assumed. One assumption maximizes the area occupied by ionomer when adsorbed, but minimizes the aggregate size change due to adsorption. The other minimizes the area occupied, but maximizes the aggregate size change. Although these assumptions are not likely true, it is possible that the final result may between these hypotheses.

6.3.1 Spherical Ionomer molecule

If a spherical geometry is assumed for ionomer molecules, then the diameter would be the measured hydrodynamic diameter from DLS. Such a sphere, when adsorbed on the Pt/CB surface would occupy an area equal to its projected area. A surface coverage was

constructed based on this assumption and adsorption data between 0g/L to 3g/L ionomer equilibrium concentration. The result is shown in figure 6-7 below:

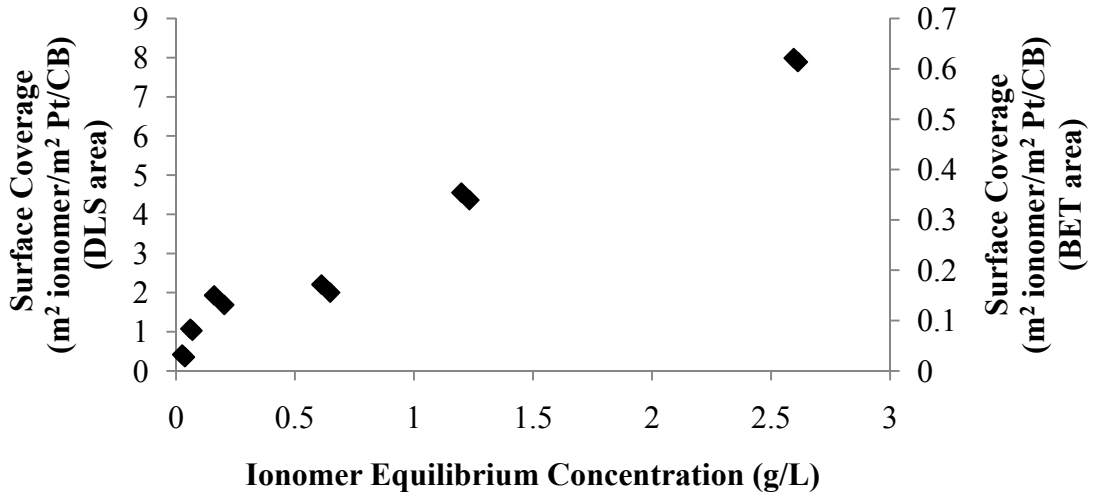

Figure 6-7 Surface coverage estimation based on DLS measurement data. Primary vertical axis represents frational surface coverage estimated based on DLS surface area ($12.4m^2/g$); secondary vertical axis represents surface coverage estimated based on BET surface area ($167m^2/g$). Ionomer molecules are assumed to be sphere particles with an average diameter around 25nm.

The surface coverage at primary adsorption plateau is around 2 if consider Pt/CB particle are spherical. In this case, the ionomer formed two layers on the Pt/Cb surface, and the total layer thickness will be twice the ionomer's diameter, which is around 50nm. The fraction surface coverage is 0.15 for BET area, which indicates that most of the Pt/CB surface was vacant at primary adsorption.

6.3.2 Rod-shape Ionomer Molecule

The ionomer molecules are rod-shaped particles with diameters around 4nm in solution [Aldebert *et al.,* 1986; Loppinet *et al.,* 1997]. Thus, calculating surface coverage based on the rod shape could provide some insight on the geometry of ionomer adsorbed on Pt/CB surface.

In a Dynamic Light Scattering measurement, the diffusion coefficient of the particle is measured and the hydrodynamic diameter is then calculated using the Stokes-Einstein equation. For a rod-shaped particle, the translational diffusion coefficient D is the orientational average of the diffusion coefficient parallel and perpendicular to the rod long axis, $D_{\parallel}$ and $D_{\perp}$ [van Bruggen *et al.,* 1997],

$$\boldsymbol{D} = \frac{\mathbf{1}}{\mathbf{3}}\boldsymbol{D}_{\parallel} + \frac{\mathbf{2}}{\mathbf{3}}\boldsymbol{D}_{\perp} \tag{6-9}$$

For diluted solutions in which the rods move without interactions and only experiencing a hydrodynamic friction with the solvent, the $D_{\parallel}$ and $D_{\perp}$ can be expressed as [Tirado *et al.,* 1984]

$$\boldsymbol{D}_{\parallel} = \frac{\boldsymbol{k_B T}}{\boldsymbol{2\pi\eta_m L}}\left[\boldsymbol{ln}\left(\frac{\boldsymbol{L}}{\boldsymbol{D}}\right) - \mathbf{0.207} + \mathbf{0.980}\frac{\boldsymbol{D}}{\boldsymbol{L}} - \mathbf{0.133}\left(\frac{\boldsymbol{D}}{\boldsymbol{L}}\right)^{\mathbf{2}}\right] \tag{6-10}$$

$$\boldsymbol{D}_{\perp} = \frac{\boldsymbol{k_B T}}{\boldsymbol{4\pi\eta_m L}}\left[\boldsymbol{ln}\left(\frac{\boldsymbol{L}}{\boldsymbol{D}}\right) + \mathbf{0.839} + \mathbf{0.815}\frac{\boldsymbol{D}}{\boldsymbol{L}} + \mathbf{0.233}\left(\frac{\boldsymbol{D}}{\boldsymbol{L}}\right)^{\mathbf{2}}\right] \tag{6-11}$$

where η_m is the viscosity of the medium, L is the length of the rod and D is the diameter of the rod, k_B is the Boltzmann's constant and T is the absolute temperature. Combining the above three equations:

$$\boldsymbol{D = \frac{k_B T}{3\pi\eta_m L}\left[ln\left(\frac{L}{D}\right) + 0.316 + 0.5825\frac{D}{L} + 0.050\left(\frac{D}{L}\right)^2\right]} \quad (6\text{-}12)$$

If the diffusion coefficient is replaced by the Stokes-Einstein equation 6-10 becomes:

$$\boldsymbol{\frac{kT}{6\pi\eta R_H} = \frac{kT}{3\pi\eta L}\left[ln\left(\frac{L}{D}\right) + 0.316 + 0.5825\frac{D}{L} + 0.05\left(\frac{D}{L}\right)^2\right]} \quad (6\text{-}13)$$

Applying D = 4nm and R_H = 12.5nm, the length of the rod was solved to be 85nm.

Considering the adsorption of such rod-shaped ionomer molecules on the Pt/CB surface in molecular form, with the geometry data, results in two cases:

1. Single molecule adsorption, where ionomer molecules are adsorbed on the Pt/CB surface parallel to rod long axis.
2. Single molecule adsorption, where ionomer molecules are adsorbed on Pt/CB surface perpendicular to rod long axis.

In the first case, the area occupied by a single ionomer molecule when adsorbed on Pt/CB surface is maximal. In the second case, the area occupied by a single ionomer molecule when adsorbed on Pt/CB surface will be minimal. The estimated result is shown in figure 6-8. In the first case, where adsorption is parallel to the ionomer rod long axis, the area

occupied by a single ionomer molecule when adsorbed on Pt/CB surface is at maximum, and the consequential Pt/CB particle size change due to ionomer adsorption is at minimum (~4nm). The surface coverage at the primary adsorption plateau is around 1.2 (DLS area) and 0.1 (BET area). In the DLS area case the entire Pt/CB surface is covered by ionomer. On the opposite, in the BET area case, most Pt/CB surface areas are not bound by ionomer, which could be areas contributed by nanopores of the Pt/CB particles. In the second case, where adsorption is perpendicular to the ionomer long axis, the ionomer adsorption area is at minimum. Such a binding orientation would result in a diameter change around 85nm, which is greater than the diameter change detected by DLS measurement (30nm-40nm). This suggests that only fraction of the ionomer rod was adsorbed on the Pt/CB surface and the rest part of the ionomer rod was pointing away from the Pt/CB surface.

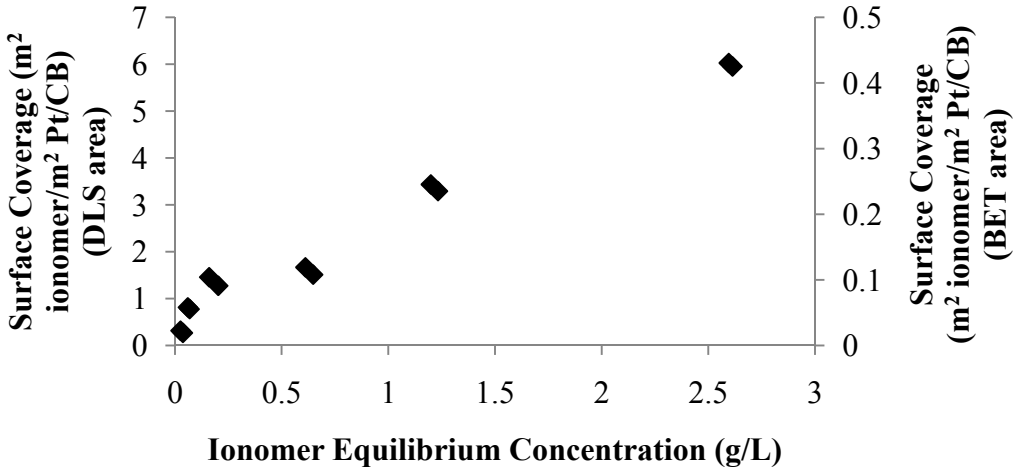

(a)

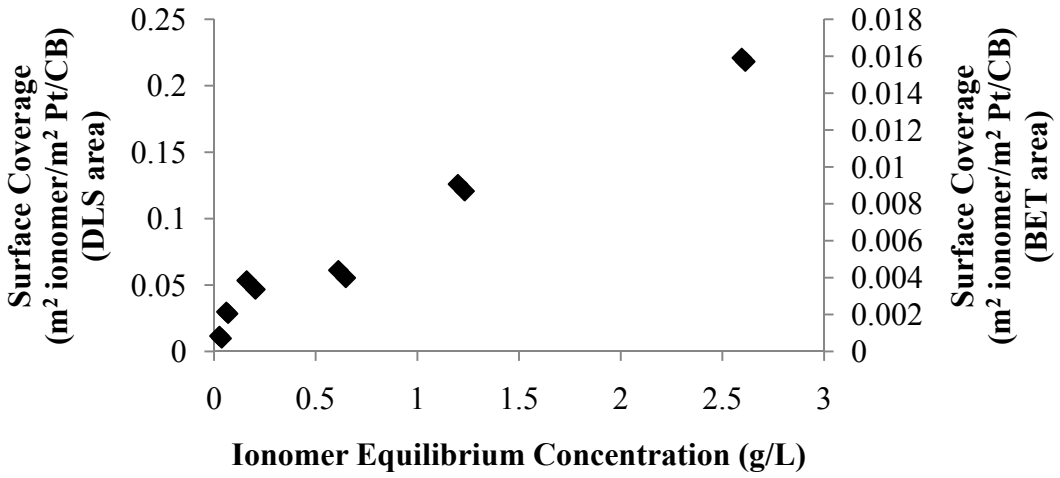

(b)

Figure 6-8 Surface coverage based on rod-shaped ionomer molecules: (a) ionomer adsorbed on Pt/CB surface parallel to the long axis; (b) ionomer adsorbed on the Pt/CB perpendicular to the long axis.

6.4 Summary

The interactions between ionomer and Pt/CB particle in solution were investigated by ^{19}F NMR and dynamic light scattering. Ionomer adsorption on Pt/CB surface was found to comprise two adsorption stages. A primary adsorption started at low concentration, and ionomer adsorbing on Pt/CB surface analog a Langmuir isotherm. An adsorption plateau was observed at 0.65 g/L ionomer equilibrium concentration and a maximum surface coverage Γ_{max} was found around 2.66 $x10^{-3}$ g/m^2. A secondary adsorption started after the

primary adsorption plateau was achieved. The primary adsorption involves adsorption of ionomer on carbon black surface, and the secondary adsorption might involves the impregnation of ionomer into nanopores of Pt/CB particles, adsorbed on platinum particles or interactions with the adsorbed primary layer.

Hydrodynamic size change of Pt/CB particles due to ionomer adsorption was examined and associated with adsorption behaviour. At low ionomer concentration, where primary adsorption occurred, the particle size of Pt/CB increased as more ionomer adsorbed on it. When adsorption plateau ended and secondary adsorption started, the effect of ionomer adsorption on particle size change became small, and the size change reached a plateau around 40nm. It is possible that the rapid particle size change at low ionomer concentration is due to primary adsorption of ionomer onto carbon black surface of Pt/CB particles. At higher ionomer concentration region that secondary adsorption occurred, ionomer adsorbed on Pt/CB particles might impregnation into nanopores of the particle or formed tightly packed arrangement on primary layer, which does not contribute a lot to the size change of the Pt/CB particles.

The geometry of ionomer molecules in solution was estimated to help understanding the adsorption. A rod shaped particle with 4nm in diameter and 85nm in length was assigned to ionomer molecule by approximation of diffusion coefficient of the molecule. The

surface coverage was calculated based on different adsorption scenarios. When considering Pt/CB particle to be spherical, the cases which ionomer adsorbed on Pt/CB as spherical and rod-shaped particle along the backbone have coverage at primary adsorption plateau greater than 1, suggesting monolayer or multiple layers of ionomer adsorbed on Pt/CB. However, if we consider Pt/CB as an irregular shaped particle, the surface coverage is always considerably less than 1, indicating that most of the Pt/CB surface is vacant. In the scenario where rod-shaped ionomer particle adsorbed on Pt/CB surface at it tip, the resulted particle size change is greater than that measured by DLS, suggesting that only a fraction of ionomer molecule is in contact with the particle surface.

Chapter 7

7.1 Conclusion

Aggregation behaviours of ionomer and carbon black support of Pt/CB particles in solution, and interactions between ionomer and Pt/CB were investigated in this thesis. The project was developed to help forge an understanding of the catalyst ink properties and to move toward the development of a microstructure model of the catalyst layer that maximizes the electrochemical active area.

Perfluorosulfonic acid-PTFE copolymer (Nafion^{TM}) in 1-propanol/water solution from 0.1wt% to 10wt% was found exist in three aggregation forms: molecular chains with hydrodynamic diameter between 20nm to 30nm, primary aggregates with hydrodynamic diameter around 300nm, and secondary aggregates with diameter above 1000nm. Between 0.1wt% and 3wt%, ionomer mainly exist in molecular form; from 3wt% to 5wt%, most ionomer molecular chains aggregate to form primary aggregates. Above 5wt%, the majority of ionomer exist as primary aggregates. Secondary aggregates exist in all concentrations.

1-propanol and 3-methyl-1-butabol were found to better dissolve ionomer among the solvents selected. When mixing water with other solvents used in this project to dissolve

ionomer, only 1-propanol and isopropanol were found to be miscible. 1-propanol/water mixtures dissolve ionomer better than isopropanol/water mixtures at all mixing ratios.

Vulcan XC-72 Carbon black support for Pt/CB particles were found finely dispersed in solvent after 2hr of sonication. Further sonication does not have a significant influence on particle size distribution. 1-propanol/water was found to disperse CB well when water content in the co-solvent mixture is less than 50wt%. A comparison of particle size distribution of carbon black and Pt/CB (10wt% Pt) at 0.01wt% concentration shows very similar results.

Adsorption of ionomer on the 10wt% Pt/CB surface comprises two adsorption stages. Primary adsorption at low ionomer concentration follows a Langmuir isotherm. Secondary adsorption starts when primary adsorption plateau reached. Pt/CB particle size changes due to ionomer adsorption increase with concentration. It is probably that ionomer adsorbed on the carbon black surface of Pt/CB particles in primary adsorption leads to Pt/CB particle size change. Secondary adsorption could be ionomer impregnated into the nanopores of Pt/CB particle or formed tightly packed structure, which contribute less to the size change.

The geometry of the ionomer molecules was modeled as a rod-shaped particle with diameter of 4nm and length of 85nm. Comparison of different adsorption scenarios with DLS measurement results suggests only a fraction of ionomer molecule is in contact with the Pt/CB surface when adsorbed.

7.2 Recommendations

7.2.1 Hansen Solubility Parameter

Hildebrand solubility parameters were used in Chapter 4 to compare solvents for ionomer. A more precise prediction of ionomer solubility could be achieved if the Hansen solubility parameter value for ionomer could be calculated.

Segarceanu et al., [1997] have devised a method to calculate the polymer HSP from data of its intrinsic viscosity in different solvents. Intrinsic viscosity will be higher in better solvents due to greater interaction and greater polymer chain extension. The intrinsic viscosity value gives an indication of the solvent quality. Intrinsic viscosities of the solution are normalized by the intrinsic viscosity of that solvent at the highest value, which has then been substituted in the equations that apply weight average to access the centre of the Hansen sphere:

$$\boldsymbol{\delta_D^{polymer}} = \sum\left(\boldsymbol{\delta_D^i} \times \boldsymbol{\eta^i}\right) / \sum \boldsymbol{\eta^i} \qquad (7\text{-}1)$$

$$\boldsymbol{\delta_P^{polymer}} = \sum\left(\boldsymbol{\delta_P^i} \times \boldsymbol{\eta^i}\right)/\sum \boldsymbol{\eta^i} \tag{7-2}$$

$$\boldsymbol{\delta_H^{polymer}} = \sum\left(\boldsymbol{\delta_H^i} \times \boldsymbol{\eta^i}\right)/\sum \boldsymbol{\eta^i} \tag{7-3}$$

Where *i* indicates the *ith* component, and the intrinsic viscosity of solvent *i* is given by η^i.

Hansen [2000] used a three-dimensional model to illustrate polymer solubility. The model is shown in figure 7-1 [Burke, 1984]. By doubling the dispersion parameter axis, an approximately spherical volume of solubility would be formed for each polymer. This sphere can be described, as the coordinates at the center of the solubility sphere are located by means of three component parameters (δ_D, δ_P, δ_H), and the radius of the sphere is indicated; this is referred to as the interaction radius (R_o).

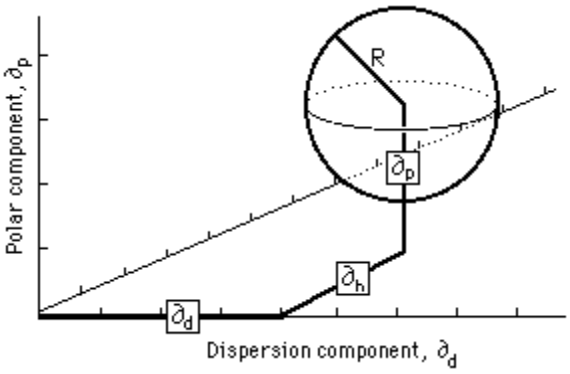

Figure 7-1 Illustration of Hansen sphere [Burke, 1984]

To determine if the polymer is able to dissolve in a solvent with a given Hansen solubility parameter, the following equation is used:

$$(\boldsymbol{R_a})^2 = \mathbf{4}(\boldsymbol{\delta_{D2}} - \boldsymbol{\delta_{D1}})^2 + (\boldsymbol{\delta_{P2}} - \boldsymbol{\delta_{P1}})^2 + (\boldsymbol{\delta_{H2}} - \boldsymbol{\delta_{H1}})^2 \quad (7\text{-}4)$$

$$\boldsymbol{RED} = {}^{\boldsymbol{R_a}}/_{\boldsymbol{R_o}} \quad (7\text{-}5)$$

Where R_a is the distance between the Hansen solubility parameter in Hansen space and 2, 1 represent polymer and solvent. The ratio RED gives an estimate of how well the given solvent dissolves the polymer:

RED < 1 the molecules are alike and will dissolve

RED = 1 the system will partially dissolve

RED > 1 the system will not dissolve

7.2.2 Ionomer Molecular Weight

Nafion^{TM} has a wide molecular weight distribution between 10^5 and 10^6 g/mol [Mauritz *et al.,* 2004]. Static light scattering and gel permeation chromatography were used to estimate the molecular weight of the ionomer used in this thesis. However, both methods were not applicable. A precise ionomer molecular weight could provide a better estimation of the ionomer's real geometry in solution, aggregation status and surface coverage of Pt/CB particle.

Bibliography

Aldebert, Pierre., Dreyfus, Bernard., Pineri, Michel. Small-Angle Neutron Scattering of Perfluorosulfonated Ionomers in Solution. *Macromolecules,* 1986, 19, 2651-2653.

Andújar, J.M., Segura, F. Fuel cells: History and updating. A walk along two centuries. *Renewable and Sustainable Energy Reviews*, 2009, 13, 2309-2322.

Arrio, Bernerd., Johannin, Georges., Carrette, Alain., Chevallier, Jean., Brethes, Daniel. Electrokinetic and Hydrodynamic Properties of Sarcoplasmic Reticulum Vesicles: A Study by Laser Doppler Electrophoresis and Quasi-Elastic Light Scattering, *Archives of Biochemistry and Biophysic*s, 1984, 223, 220-229

Baghalha, M., Stumper, J., Harvey, D., Eikerling, M. Modeling the effect of low carbon conductivity of the cathode catalyst layer on PEM fuel cell performance. *ECS Transactions,* 2010, 28, 113-123.

Burke, John. Solubility Parameters: Theory and Application, *AIC Book and Paper Group*. *Annual*, 1984, 3, 13-58.

Chen, Hong., Snyder, Joshua D., Elabd, Yossef A. Electrospinning and Solution Properties of Nafion and Poly(acrylic acid). *Macromolecules*, 2008, 41, 128-135

Cheng, Xiaoliang., Yi, Baolian., Han, Ming., Zhang, Jingxin., Qiao, Yaguang., Yu, Jingrong. Investigation of platinum utilization and morphology in catalyst layer of polymer electrolyte fuel cells. *Journal of power sources,* 1999, 79, 75-81

Cirkel, Peter A., Okada, Tatsuhiro., Kinugasa, Shinichi. Equilibrium Aggregation in Perfluorinated Ionomer Solutions. *Macromolecules,* 1999, 32, 531-533.

Chu, B. *Soft Matter Characterization.* Springer Netherlands, 2008.

Chu, Deryn., Jiang, R., Gardner, K., Jacobs, R., Schmidt, J., Quakenbush, T., Stephens , J. Polymer electrolyte membrane fuel cells for communication applications. *Journal of power sources,* 2001, 96, 174-178.

Cleghorn, S. J. C., Ren, X.., Springer, T. E., Wilson, M. S., Zawodzinski, C., Zawodzinski, T. A., Gottesfeld, S. Pem fuel cells for transportation and stationary power generation applications. *International Journal of Hydrogen Energy*, 1997, 22, 1137-1144.

Deluca, Nicholas W., Elabd, Yossef A. Polymer Electrolyte Membranes for the Direct Methanol Fuel Cell: A Review. *Journal of Polymer Science: Part B: Polymer Physics,* 2006, 44, 2201–2225

Dubin, P., Bock, J., Davis, R., Schulz, Donald N. *Macromolecular Complexes in Chemistry and Biology*. Springer Verlag: New York, 1994.

Du, Heng. Mie-scattering calculation, *Applied Optics,* 2004, 43, 1951-1956.

Farhat, Zoheir **N.** Modeling of catalyst layer microstructural refinement and catalyst utilization in a PEM fuel cell. *Journal of power sources,* 2004, 138, 68-78.

Fernández, R., Ferreira-Aparicio, P., Daza, L. PEMFC electrode preparation: Influence of the solvent composition and evaporation rate on the catalytic layer microstructure. *Journal of power sources,* 2005, 151, 18-24.

Frey, Th., Linardi, M. Effects of membrane electrode assembly preparation on the polymer electrolyte membrane fuel cell performance. *Electrochimica Acta,*2004, 50, 99–105.

Gharagheizi, F. New procedure to calculate the Hansen solubility parameters of polymers, *Journal of Applied Polymer Science*, 2007, 103, 31–36.

Grigoriev, S.A., Lyutikova, E.K., Martemianov, S., Fateev, V.N. On the possibility of replacement of Pt by Pd in a hydrogen electrode of PEM fuel cells. *International Journal of Hydrogen Energy*, 2007, 32, 4438 – 4442.

GoldBurg, W.I. Dynamic Light Scattering, *Am. J. Phys*, 1999, 67(12), 1152-1160.

Hansen, C. M. The Three Dimensional Solubility Parameter - Key to Paint Component Affinities I, *J. Paint Technol.,* 1967, 39, 104–117.

Hansen, C. M., The Three Dimensional Solubility Parameter - Key to Paint Component Affinities II, *J. Paint Technol.,* 1967, 39, 505–510.

Hansen, C. M., Skaarup, K. The Three Dimensional Solubility Parameter - Key to Paint Component Affinities III, *J. Paint Technol.,* 1967, 39, 511–514.

Hansen, Charles M, *Hansen's solubility parameters: a user's handbook*, Taylor & Francis Group, 2000.

Henry, D.C. The Cataphoresis of Suspended Particles. Part I. The Equation of Cataphoresis, *Proc. R. Soc. Lond*, *1931, 131, 106*-129.

Herráez, J.V., Belda, R. Viscous Synergy of Pure Monoalcohol Mixtures in Water and its Relation to Concentration, *Journal of Solution Chemistry*, 2004, 33, 117-129.

Hiemenz, Paul C., Rajagopalan, Raj. *Principles of Colloid and Surface Chemistry*. Marcel Dekker Inc., 1997.

Hildebrand, J. H., Scott, R. L. *Regular Solutions*. Prentice-Hall: Englewood Cliffs, NJ, 1962.

Hoogers, Gregor. *Fuel Cell Technology Handbook.* CRC Press, 2003.

Jiang, Suhong., Xia, Ke-Qing., Xu, Gu. Effect of Additives on Self-Assembling Behavior of Nafion in Aqueous Media. *Macromolecules,* 2001, 34, 7783-7788

Kamarajugadda, Sai., Mazumder, Sandip. Numerical investigation of the effect of cathode catalyst layer structure and composition on polymer electrolyte membrane fuel cell performance. *Journal of power sources,* 2008, 183, 629-642.

Kang, Yongyin., Ren, Mingjun., Zou, Zhiqing., Huang, Qinghong., Li, Zhilin., Akins, Daniel L., Yang, Hui. Improved electrocatalytic performance of Pd nanoparticles with size-controlled Nafion aggregates for formic acid oxidation, *Electrochimica Acta*, 2010, 55, 5274–5280.

Karyakin, AA., Morozov, SV., Karyakina, EE., Varfolomeyev, SD., Zorin, NA., Cosnier, S. Hydrogen fuel electrode based on bioelectrocatalysis by the enzyme hydrogenase. *Electrochem Commun,* 2002, 4, 417–420.

Kaszuba, Michael., McKnight, David., Connah, Malcolm T., McNeil-Watson, Fraser K., Nobbmann, Ulf. Measuring sub nanometre sizes using dynamic light scattering, *J Nanopart Res,* 2008, 10, 823–829.

Khajeh-Hosseini-Dalasm, N., Kermani, M.J., Ghadiri Moghaddam, D., Stockie, J.M. A parametric study of cathode catalyst layer structural parameters on the performance of a PEM fuel cell. *International Journal of Hydrogen Energy*, 2010, 35, 2417 – 2427.

Kim, Joon-Hee., Ha, Heung Yong., Oh, In-Hwan., Hong, Seong-Ahn., Lee, Ho-In. Influence of the solvent in anode catalyst ink on the performance of a direct methanol fuel cell. *Journal of Power Sources*, 2004, 135, 29–35.

Komoda, Yoshiyuki., Okabayashi, Ko., Nishimura, Hironobu., Hiromitsu, Masashi., Oboshi Takanori., Usui, Hiromoto. Dependence of polymer electrolyte fuel cell performance on preparation conditions of slurry for catalyst layers, *Journal of Power sources,* 2009, 193, 488-494.

Kreuer, K.D. On the development of proton conducting polymer membranes for hydrogen and methanol fuel cells. *Journal of Membrane Science,*2001, 185, 29-39.

Lee, Su-Jen., Yu, T Leon., Lin, Hsiu-Li., Liu, Wen-Horng., Lai, Chen-Lan. Solution properties of nafion in methanol/water mixture solvent. *Polymer,* 2004, 45, 2853-2862.

Lin, Hsiu-Li., Yu, T. Leon., Huang, Cheng-Hung., Lin, Tsang-Lang. Morphology study of Nafion membranes prepared by solutions casting, *Journal of Polymer Science Part B: Polymer Physics,* 2005, 34, 3044-3057.

Lin, Hsiu-Li., Yu, T. Leon., Huang, Li-Ning., Chen, Li-Chung., Shen, Kun-Sheng., Jung Guo-Bin. Nafion/PTFE composite membranes for direct methanol fuel cell applications, *Journal of Power Sources,* 2005, 150, 11-19.

Litster, S., Mclean, G. PEM fuel cell electrodes. *Journal of Power Sources,* 2004, 130, 61-76.

Loppinet, Benoit., Gebel, Ge´rard., Williams, Claudine E. Small-Angle Scattering Study of Perfluorosulfonated Ionomer Solutions. *J. Phys. Chem. B,* 1997, *101,* 1884-1892.

Ma, Chia-Hung., Yu, T. Leon., Lin, Hsiu-Li., Huang, Yu-Ting., Chen, Yi-Ling., Jeng, U-Ser., Lai, Ying-Huang., Sun, Ya-Sen. Morphology and properties of Nafion membranes prepared by solution casting, *Polymer*, 2009, 50, 1764-1777.

Ma, Shuang., Chen, Qian., Jøgensen, Fleming H., Stein, Paul C., Skou, Eivind M. ^{19}F NMR studies of Nafion™ ionomer adsorption on PEMFC catalysts and supporting carbons, *Solid State Ionics*, 2007, 178, 1568–1575.

Malvern Technical Support Library, How is distribution calculated in DLS, http://www.malvern.com/malvern/kbase.nsf/allbyno/KB000820/$file/FAQ%20-%20How%20is%20the%20distribution%20calculated%20in%20DLS.pdf.

Marr, Curtis., Li, Xianguo. Composition and performance modelling of catalyst layer in a proton exchange membrane fuel cell. *Journal of Power Sources,* 1999, 77, 17-27.

Maurer-Spurej, Elisabeth., Brown, Keddie., Labrie, Audrey., Marziali, Andre., Glatter, Otto. Portable dynamic light scattering instrument and method for the measurement of blood platelet suspensions. *Phys. Med. Biol.* 2006, 51, 3747–3758.

Mauritz, Kenneth A., Moore, Robert B. State of Understanding of Nafion, *Chem. Rev.* 2004, 104, 4535-4585.

Mie, G. Contributions on the optics of turbid media, particularly colloid metal solutions, *Annals of physics,* 1908, 330, 377-445.

Mikhail, S. Z., Kimel, W. R. Densities and Viscosities of 1-Propanol-Water Mixtures, *Journal of Chemical and Engineering Data*, 1963, 8, 323-328.

Millett, S., Mahadevan., K. Commercialization scenarios of polymer electrolyte membrane fuel cell applications for stationary power generation in the United States by the year 2015, *Journal of Power Sources*, 2005,150, 187–191.

O'Hayre, Ryan. P., Cha, Suk-Won., Collela, Whitney. G., Prinz, Fritz. B. *Fuel Cell Fundamentals, 2nd Edition.* John Wiley & Sons Inc, 2009.

Pan, Jingjing., Zhang, Haining., Pan, Mu. Self-assembly of Nafion molecules onto silica nanoparticles formed in situ through sol–gel process, *Journal of Colloid and Interface Science*, 2008, 326, 55–60.

Patterson, D., Delmas, G. New aspects of polymer solution thermodynamics, *Off Dig Fed Soc Paint Technol*, 1962, 34, 677-681.

Penner, S. S., Appleby, A. J., Baker, B. S., Bates, J. L., Buss, L. B., Dollard, W. J., Fartis, P. J., Gillis, E. A., Gunsher, J. A., Khandkar, A., Krumpelt, M., O'Sullivan, J. B., Runte, G., Savinell, R. F., Selman, J. R., Shores, D. A., Tarman, P. Commercialization of fuel cells. *Energy*, 1995, 20, 331-470.

Prater, Keith. B. Polymer electrolyte fuel cells: a review of recent developments. *Journal of Power sources,* 1994, 51, 129-144.

Ramya, K., Velayutham, G., Subramaniam, C.K., Rajalakshmi, N., Dhathathreyan, K.S. Effect of solvents on the characteristics of Nafion®/PTFE composite membranes for fuel cell applications, *Journal of Power Sources,* 2006, 160, 10-17.

Russel, W.B., Saville, D.A., Schowalter, W.R. *Colloidal Dispersions*, Cambridge University Press, 1989

Schlick, Shulamith., Gebel, J Gerard., Pineri, Michel., Volinot, Ferdinand. ^{19}F NMR Spectroscopy of Acid Nafion Membranes and Solutions, *Macromolecules*, 1991, 24, 3517-3521.

Shen, Jianqi., Cai, Xiaoshu. Algorithm of Numerical Calculation on Lorentz Mie Theory, *Progress In Electromagnetics Research Symposium*, 2005, 22, 691-694.

Shin, S.J., Lee, J.K., Ha, H.Y., Hong, S.A., Chun, H.S., Oh, I.H. Effect of the catalytic ink preparation method on the performance of polymer electrolyte membrane fuel cells. *Journal of Power Sources,* 2002, 106, 146-152.

Sohn, Seungman., Kim, Dongsu. Modification of Langmuir isotherm in solution systems - Definition and utilization of concentration dependent factor, *Chemosphere*, 2005, 58, 115-123.

Song, Datong., Wang, Qianpu., Liu, Zhongsheng., Navessin, Titichai., Eikerling, Michael., Holdcroft, Steven. Numerical optimization study of the catalyst layer of PEM fuel cell cathode. *Journal of Power sources,* 2004, 126, 104-111.

Stampino, Paola Gallo., Cristiani, Cinzia., Dotelli, Giovanni., Omati, Luca., Zampori, Luca., Pelosato, Renato., Guilizzoni, Manfredo. Effect of different substrates, inks composition and rheology on coating deposition of microporous layer (MPL) for PEM-FCs. *Catalyst Today,*2009, 147S, S30-S35.

Szajdzinska-Pietek, Ewa., Schlick, Shulamith., Plonka, Andrzej, Self-Assembling of Perfluorinated Polymeric Surfactants in Nonaqueous Solvents. Electron Spin Resonance Spectra of Nitroxide Spin Probes in Nafion Solutions and Swollen Membranes, *Langmuir*, 1994, 10, 2188-2196

Tandon, Vishal., Bhagavatula, Sharath K., Nelson, Wyatt C., Kirby, Brian J. Zeta potential and electroosmotic mobility in microfluidic devices fabricated from hydrophobic polymers: 1. The origins of charge, *Electrophoresis,* 2008, 29*,* 1092–1101

Taylor, Andr´e D., Kim, Edward Y., Humes, Virgil P., Kizuka, Jeremy., Thompson, Levi T. Inkjet printing of carbon supported platinum 3-D catalyst layers for use in fuel cells. *Journal of Power Sources,* 2007, 171, 101-106.

Tirado, M. M., Martinez, C. L., de la Torre, J. G. Comparison of theories for the translational and rotational diffusion coefficients of rod-like macromolecules. Application to short DNA fragments, *J. Chem. Phys*, 81, 1984, 2047-2052.

Uchida, Makoto., Aoyama, Yuko., Eda, Nobuo., Ohta, Akira. Investigation of the Microstructure in the Catalyst Layer and Effects of Both Perfluorosulfonate Ionomer and PTFE-Loaded Carbon on the Catalyst Layer of Polymer Electrolyte Fuel Cells. *J. Electrochem. Soc.,* 1995, 142, 4143-4149.

Uchida, Makoto., Fukuoka, Yuko., Sugawara, Yasushi., Ohara, Hideo., Ohta, Akira. Improved Preparation Process of Very-Low-Platinum-Loading Electrodes for Polymer Electrolyte Fuel Cells. *J. Electrochem. Soc.,* 1998, 145, 3708-3713.

Van Bruggen, M. P. B., Lekkerkerker, H. N. W., Dhont, J. K. G. Long-time translational self-diffusion in isotropic dispersions of colloidal rods, *Physical Review E*, 1997, 56, 4394-4403.

Van Der Hoeven, Ph. C., Lyklema, J. Electrostatic stabilization in non-aqueous media, *Advances in Colloid and Interface Science*, 1992, 42, 205-277.

Van de Hulst, H.C. *Light Scattering by Small Particles*, Wiley, New York, 1957.

Wang, B. Recent development of non-platinum catalysts for oxygen reduction reaction, *Journal of Power Sources*, 2005, 152, 1–15.

Wang, Suli., Sun, Gongquan., Wu, Zhimou., Xin, Qin, Effect of Nafion® ionomer aggregation on the structure of the cathode catalyst layer of a DMFC, *Journal of Power Sources,* 2007, 165, 128-133.

Wang, Qianpu., Eikerling, Michael., Song, Datong., Liu**,** Zhongsheng. Structure and performance of different types of agglomerates in cathode catalyst layers of PEM fuel cells. *Journal of Electroanalytical Chemistry*, 2004, 573, 61–69.

Wannek, Christoph., Glüsen, Andreas., Stolten, Detlef. Materials, manufacturing technology and costs of fuel cell membranes. *Desalination,* 2010, 250, 1038-1041.

Ware, B. R. Electrophoretic Light Scattering, *Advances in Colloid and Interface Science*, 1974, 4, 1-44.

Wilson, MS., Gottesfeld, S. Thin-film catalyst layers for polymer electrolyte fuel cell electrodes, *J Appl Electrochem*, 1992, 22, 1-7.

Wiscombe, W.J. Improved Mie scattering algorithms, *Applied Optics,* 1980, 19, 1505-1509.

Wu, C.; Woo, K.; Jiang, M. Light-Scattering Studies of Styrene−(Ethylene-*co*-butylene)−Styrene Triblock Copolymer and Its Sulfonated Ionomers in Tetrahydrofuran, *Macromolecules* 1996, 29, 5361-5367.

Xie, Jian., Garzon, Fernando., Zawodzinski, Thomas., Smit, Wayne. Ionomer Segregation in Composite MEAs and Its Effect on Polymer Electrolyte Fuel Cell Performance, *Journal of The Electrochemical Society*, 2004, 151, A1804-A1903.

Xu, Renliang., Wu, Chifei., Xu, Haiyan. Particle size and zeta potential of carbon black in liquid media, *Carbon*, 2007, 45, 2806-2809.

Yeo, Richard S. Dual cohesive energy densities of perfluorosulphonic acid (Nafion) membrane, *Polymer*, 1980, 21, 432-435.

Zhang, Haining., Pan, Jingjing., He, Xiuchong., Pan, Mu. Zeta Potential of Nafion Molecules in isopropanol-Water Mixture Solvent, *Journal of Applied Polymer Science,* 2008, 107, 3306–3309.

Zeta potential measurement using laser Doppler electrophoresis (LDE), Malvern Instrument, http://www.malvern.com/LabEng/technology/zeta_potential/zeta_potential_LDE.htm.